Fermi National Accelerator Laboratory

FERMILAB-Pub-78/57-EXP
7420.045

(Submitted to Phys. Rev. D)

EXPERIMENTAL STUDY OF HADRONS PRODUCED IN HIGH ENERGY CHARGED CURRENT NEUTRINO-PROTON INTERACTIONS

J. Bell, C. T. Coffin, R. N. Diamond, H. T. French, W. C. Louis, B. P. Roe, R. T. Ross, A. A. Seidl, J. C. Vander Velde, and E. Wang
University of Michigan, Ann Arbor, Michigan 48109

and

J. P. Berge, D. V. Bogert, F. A. DiBianca, R. Endorf, R. Hanft, C. Kochowski, J. A. Malko, G. I. Moffatt, F. A. Nezrick, W. G. Scott, and W. Smart
Fermi National Accelerator Laboratory, Batavia, Illinois 60510

and

R. J. Cence, F. A. Harris, M. Jones, M. W. Peters, V. Z. Peterson, and V. J. Stenger
University of Hawaii at Manoa
Honolulu, Hawaii 96822

and

G. R. Lynch, J. P. Marriner, and M. L. Stevenson
Lawrence Berkeley Laboratory, Berkeley, California 94720

July 1978

Experimental Study of Hadrons Produced in High Energy Charged Current Neutrino-Proton Interactions

J. Bell, C.T. Coffin, R.N. Diamond[†], H.T. French[‡], W. C. Louis, B.P. Roe, R.T. Ross, A.A. Seidl, J.C. Vander Velde, E. Wang

University of Michigan
Ann Arbor, Michigan 48109

J.P. Berge, D.V. Bogert, F.A. DiBianca[§], R. Endorf[#], R. Hanft, C. Kochowski[*], J.A. Malko, G.I. Moffatt[#], F.A. Nezrick, W.G. Scott[††], W. Smart

Fermi National Accelerator Laboratory
Batavia, Illinois 60510

R.J. Cence, F.A. Harris, M. Jones, M.W. Peters, V.Z. Peterson, V. J. Stenger

University of Hawaii at Manoa
Honolulu, Hawaii 96822

G.R. Lynch, J.P. Marriner, M.L. Stevenson

Lawrence Berkeley Laboratory
Berkeley, CA. 94720

[†]Present address: Florida State University, Tallahassee, Fl. 32306

[‡]Present address: Columbia University, New York, N.Y. 10027

[§]Present address: General Electric Company, Milwaukee, Wis.

[#]Visitors from the University of Cincinnati

[*]Present address: CEN Saclay, France

[††]Present address: CERN, Geneva 23, Switzerland

ABSTRACT

We analyze a sample of about 2000 charged-current neutrino-proton interactions with neutrino energy greater than 10 GeV produced in the 15-ft. hydrogen bubble chamber at Fermilab using a broad band neutrino beam. We study the details of the hadrons produced and find generally good agreement with the quark-parton model and present parameterizations of quark fragmentation (D) functions. The D functions are found to be independent of Q^2 and W (total hadronic mass) for $W > 4$ GeV, in agreement with the model. The height of the rapidity plateau in the quark (current) fragmentation region is compared to that of the di-quark (target) fragmentaion region and the two are found to agree. Detailed charge correlation data are presented and compared to the Field-Feynman model of the D functions, and also to a longitudinal phase space model, and are found to disagree with both. The mean transverse momentum P_T of the hadrons is studied for its Q^2 and Feynman-X dependence. We find a sizeable increase of $\langle P_T^2 \rangle$ with Feynman-X which agrees, however, with our longitudinal phase space model. We find no statiscally significant dependence of $\langle P_T^2 \rangle$ on Q^2, up to $Q^2 = 64$ GeV^2, although the highest momentum hadrons are consistent with a mild Q^2 dependence. The azimuthal angular distribution of the highest momentum hadrons in high Q^2 events is examined for evidence of anisotropy of the type that has been predicted for effects of gluon radiation.

I INTRODUCTION

According to commonly accepted models of the weak interaction, the inelastic process $\nu p \rightarrow \mu^- +$ hadrons occurs via the exchange of a virtual intermediate W^+ boson. In the quark-parton model, the W^+ can strike a valence d-quark in the proton and change it to a u-quark, which then "fragments" into the observed hadrons:

$$W^+ + d \rightarrow u \rightarrow \text{hadrons}. \qquad (1)$$

The way in which a given quark fragments into hadrons is a fundamental aspect of the quark-parton model which must be determined from experiment.[1] In neutrino charged current interactions a pure u-quark state is formed (when the Bjorken scaling variable x is not too small) thereby allowing one to study how this pure state disintegrates.

It is the purpose of this paper to investigate, within the context of the quark-parton model, the functions which describe the fragmentation of a u-quark into $\pi^\pm$ mesons; and, generally, to present details about the produced hadronic state. The data are based on a 150,000 picture exposure of the FNAL 15-foot hydrogen bubble chamber to a wide-band neutrino beam. Some of the general features of an early subset of the data have been published elsewhere.[2,26]

We begin with the usual definition[3] of the quark fragmentation functions $D_q^h(Z)$ which give the probability that a quark q will produce a hadron h having a fraction Z of the quark's total energy. (We actually define Z as the component of a given hadron's momentum in the direction of the total hadronic lab momentum, divided by that total momentum.) In a given event the total hadronic momentum and energy are completely specified by the neutrino energy E_ν and the Bjorken scaling variables $x = Q^2/2m\nu$ and $y = \nu/E_\nu$ where Q is the neutrino-muon four-momentum transfer, ν is their energy transfer, and m is the proton mass. We can write the cross section for the semi-inclusive process $\nu p \to \mu^- + h +$ anything as a sum over struck (q') and produced (q) quark states:

$$\frac{d\sigma^h}{dxdydZ} = \sum_q \left(\frac{d\sigma}{dxdy}\right)_{q' \to q} D_q^h(Z) \qquad (2)$$

(We suppress for now the P_T dependence of the D functions.) Neglecting strangeness-changing and charm-changing currents (at most ten percent of the cross section) the only quark transformations induced by the W^+ are $d \to u$ and $\bar{u} \to \bar{d}$. Hence we can write

$$\frac{d\sigma^{\pi^\pm}}{dxdydZ} = \left(\frac{d\sigma}{dxdy}\right)_{d\to u} \cdot D_u^{\pi^\pm}(Z) + \left(\frac{d\sigma}{dxdy}\right)_{\bar{u}\to\bar{d}} \cdot D_{\bar{d}}^{\pi^\pm}(Z) \qquad (3)$$

Using the charge conjugation and isospin symmetry of the D^π functions this becomes

$$\frac{d\sigma^{\pi^\pm}}{dxdydZ} = \left[\left(\frac{d\sigma}{dxdy}\right)_{d\to u} + \left(\frac{d\sigma}{dxdy}\right)_{\bar{u}\to\bar{d}}\right] \cdot D_u^{\pi^\pm}(Z) = F(x,y) \cdot D_u^{\pi^\pm}(Z) \qquad (4)$$

The factorization property of (4) is a result of the quark-parton model which predicts that the shape of the Z distribution for inclusive π production is independent of x and y, provided, at least, that the pions are fragments of the struck quark, uncontaminated by fragments of the target proton. The quark-parton model also predicts that the D functions will be independent of Q^2 and W, the total hadronic mass. In the remainder of the paper we will show evidence regarding these predictions and investigate the longitudinal and transverse momentum properties of the $D_u^{\pi^\pm}$ functions.

The Z dependence of the correlation between the quantum numbers of the fragmenting quark and those of the observed hadrons is subject to considerable theoretical uncertainty. To investigate this we will give details on how the quark charge is distributed along its momentum direction and compare the results to model calculations. We will also investigage the transverse momentum and azimuthal properties of the produced hadrons, as this is where the effects of gluon emission are likely to appear. The reader is referred to Ref. (1) for the relationship and comparison of electroproduction results to neutrino production results.

II General Features

We begin by selecting events with ≥ 3 charged prongs which have a total visible beam-direction momentum ≥ 10 GeV/c. To obtain well-measured events we require a minimum distance of 65 cm from the event vertex to the downstream wall of the bubble chamber, and require that all tracks have momentum errors ≤ 30%. The above selection results in a sample of 2560 events.

The track most likely to be the μ^- is then selected using the kinematic procedure outlined in Appendix A. We then remove events

with $P_{TR} < 1.0$ GeV/c and with $\Phi_{VIS} < 60°$; where P_{TR} is the transverse momentum of the μ^- with respect to the momentum vector $\vec{P}_{VIS}$ of all the remaining visible particles (including V°'s), and Φ_{VIS} is the azimuthal angle between the μ^- and $\vec{P}_{VIS}$ when projected onto a plane perpendicular to the beam. Monte Carlo calculations indicate that a μ^- is correctly identified in about 97% of the events in our final sample. The P_{TR} and Φ_{VIS} cuts reject about 85% of the neutral current background events, while retaining about 85% of the charged-current sample (again, indicated by Monte Carlo calculations and described in detail in Appendix A) and reduce the sample to 1928 events.

In order to determine the other kinematic variables in the events we must "reconstruct" them, i.e., determine E_ν, W, Q^2, etc. on an event-by-event basis. For this purpose the incident neutrino direction is well known in this experiment but the neutrino energy for each event is not. This means that events with unseen neutrals of unknown mass are underconstrained by one variable, assuming all visible particles are correctly identified. About 80-90% of the events we use fall into this missing-neutrals category. We reconstruct them in an approximate way by estimating the invisible beam-direction momentum based on the configuration of the visible particles. There are several methods of doing this,[7,24] one of which was used on the earlier data sample.[2] Details of our present method are given in Appendix B. Uncertainties in the reconstruction lead to errors in the variables Z, X_F (Feynman X in the W rest frame, defined as the longitudinal momentum divided by W/2) and Y_q (rapidity in the quark frame.[8,14]) These errors, which we describe in more detail in

Appendix B, are not serious for the present discussion, nor are the corresponding errors in W, Q^2, and E_ν which we will use primarily to make cuts in the data sample. In any case, we always pass our Monte Carlo events through the same analysis procedures as the real events so that the same reconstruction errors, etc., apply to both samples. This allows us to assess the average effects of the reconstruction procedure and cuts in the data sample for each quantity studied.

After the reconstruction we keep events with $E_\nu > 10$ GeV, $x > .05$ and $y < 0.9$. These cuts are used throughout the paper and are made to further reduce the background from neutral current events and $\bar{\nu}$ events. The x cut is also made to eliminate events with large reconstruction uncertainties. One further selection is made by requiring $R_{xyz} < 3$ (described in Appendix A). This cut has a high degree of overlap with the $y < .9$ selection for neutrino charged-current (CC) events and virtually eliminates anti-neutrino charged-current ($\overline{CC}$) background.[4] These cuts reduce the sample to 1670 events.

The invariant hadronic mass (W) distribution for these 1670 events is shown in Fig. 1. Outside of the prominent peak in the first two bins, which is due to the reaction $\nu p \to \mu^- \Delta^{++}$, the distribution is smooth and reflects the approximate x and y scaling properties of the interaction. (The detailed properties of the Δ^{++} reaction will be discussed elsewhere.[5])

In order to remove the Δ^{++} and production of other low-lying N^* in exclusive channels we cut out events with $W < 2$ GeV. This reduces the sample to 1474 events, 1154 of which have $2 < Q^2 < 64$ GeV and $2 < W < 10$ GeV. In Fig. 2 we show for these events the

dependence of the average charged particle multiplicity ($\langle N_{ch} \rangle$) in the hadronic system as a function of W and Q^2. There is a definite increase of $\langle N_{ch} \rangle$ with W, as can be seen from the dashed lines which give the overall $\langle N_{ch} \rangle$ for each W bin. Within each W bin there is no apparent variation with Q^2. This confirms conclusions arrived at using one-fourth of the present data [2], and has also been noted in muoproduction of hadrons at lower Q^2 and W values.[6]

In order to investigate the Feynman scaling properties (Q^2 and W independence) of the D functions we want to examine hadrons produced in the "high Z" region. We note that the D functions cannot be independent of W over their entire range, $0 < Z < 1$, since $\int_0^1 D^\pi \, dZ$ gives the average π multiplicity at that W value, and this grows with W, as seen in Fig. 2. We show in Fig. 3 the number of (±) hadrons per event with $Z > .2 \left(\int_{.2}^{1.0} D_u^\pi \, dZ \right)$ as a function of W (the total hadronic mass). We choose $Z > .2$ as the "high Z" region since for pions $Z \simeq X_F$ here, and the pion distributions approximately scale (are independent of W) in this region in hadron-hadron collisions. In the bubble chamber we are unable, generally, to distinguish charged kaons from pions, and although the overall K/π ratio is about 10%, recent electroproduction measurements[9] indicate that the ratio K^+/π^+ gets as large as .2 to .3 in the high-X_F region (with K^-/π^- about .10 to .15 .) What we actually measure is the sum $h^\pm = (\pi+K)^\pm$ with the kaons interpreted as pions by assigning the pion mass to them when calculating their energies. The resulting shift in X_F is small and has a negligible effect on our results. Electroproduction results[10] also indicate the proton contamination is negligible in the high X_F region,

and this is confirmed by comparing our observed proton spectrum with our Monte Carlo results (see Fig. 4). The D functions for $h^{\pm}$ we will refer to as $D^{\pm}$. The data of Fig. 3, even for these high-Z tracks, show a marked W dependence for small W values. This is not unexpected, since when W is at the $p\pi^+\pi^+\pi^-$ threshold one must have $D^{\pi^-} \to 0$. However for W > 4 GeV there is an onset of a plateau region for both h^+ and h^- indicating that Feynman scaling works in the high Z region for events with high W. This confirms one of the basic assumptions of the quark fragmentation model.

The solid lines on Fig. 3 are from a Monte Carlo calculation described in Appendix C. The hadronic states are generated, for a given W, according to longitudinal phase space for produced mesons plus an approximately flat distribution in X_F for the recoiling nucleon in the interval $-.95 > X_F > 0$. The Monte Carlo events are constrained to conserve energy, momentum and charge, but there are no charge-charge or charge-neutral correlations, resonances, clusters or quark decay functions built in. For this reason we refer to the calculation as an uncorrelated Monte Carlo (UMC) and will make frequent use of it throughout the paper as a benchmark to which we will compare the data. The onset of hadronic scaling seen in Fig. 3 is apparently in agreement with the "kinematic" effect of longitudinal phase space generated by the UMC.

We consider Figs. 2 and 3 to be a reasonable confirmation of the factorization property of Eq. (4) (for Z > .2 and W > 4 GeV), so we proceed to investigate the D functions[11,12] using 847 events left after the W > 4 GeV selection.

III Determination of the D Functions

In Fig. 4 we show the function D_u^+ vs. the variable X_F. We prefer X_F to Z here in order to delineate more clearly the region $X_F < .2$ which is heavily contaminated by the recoiling proton and its fragments. (For pions with $X_F > .2$, Z and X_F are essentially equal when $W > 4$ GeV.) The UMC calculation, which is absolutely normalized, gives a rather good description of the data over most of the X_F range. The effect of recoiling protons, some of which are misidentified as π^+, can be judged from the UMC curves shown on Fig. 4. The model assumes 50% of the recoiling nucleons are protons and that these can be reliably identified in the bubble chamber if their momentum is less than 1.0 GeV/c. It is seen that the model predicts approximately the correct observed proton distribution and a negligible contamination from misidentified protons for $X_F > .2$, in agreement with electroproduction data.[8]

Turning to negative hadrons, we show the function D_u^- in Fig. 5b. One notes that both h^+ and h^- are slightly asymmetric, favoring $X_F > 0$. This is the direction of the virtual W^+ boson in the c.m. of the hadronic system generated by the W^+-proton interaction. This asymmetry is reproduced by the UMC because hadrons are generated in the rest frame of a system which recoils against the outgoing nucleon (see Appendix C).

The ratio R of positive to negative hadrons is shown in Fig. 5a. The fact that R increases rapidly as $X_F \to -1$ is due, at least in part, to the proton plateau observed in Fig. 4. The increase in R as $X_F \to +1$ is of greater theoretical interest since it is predicted by models of the D functions. The UMC appears to give a

good description of the high X_F (= high Z) region, as do the models of Field and Feynman[1] and Osborne.[13] It is interesting that three such widely different approaches give such similar results.[15] In the UMC calculation the increase in R for high X_F is due to the double positive charge of the hadronic state (the average charge of the hadrons, excluding the recoil nucleon, is +1.5 per event) and the fact that the high X_F region is populated significantly by events with low multiplicity in which the effects of charge conservation are important. In the next section we will explore further how a fragmenting quark distributes its charge.

IV Charge Distribution and Correlations

Field and Feynman suggest (FF2)[16] that when a high energy quark fragments its properties will be most strongly correlated to those of the highest momentum ("fastest") hadron observed. They have made predictions for the distribution in Z_R of the fastest positive and fastest negative hadron in each event, where Z_R is the fraction of the total charged hadron momentum carried by the fastest charged hadron. These predictions for a fragmenting u-quark are shown in Fig. 6, and are in good agreement with the data. We also show the UMC calculation. It is somewhat surprising that the UMC model gives such a good description, since it has no input charge correlations other than those arising from charge conservation. The difference between the fastest positive and the fastest negative distributions in the UMC arises solely from the fact that there are more positives than negatives generated in each event, and hence the fastest one is more likely to be positive. This

difference between positives and negatives will diminish at higher W values but the predicted change with W is slow due to the logarithmic increase in charged particle multiplicity put into the UMC model. We will say more about this below.

If a leading quark develops into a hadron jet by emitting $q\bar{q}$ pairs then one might expect there to be a correlation in the charge of the fastest (h_1) and second fastest (h_2) charged hadrons in an event. The predictions of FF2 for these correlations are shown in Table I along with the data and the UMC calculations.

It is apparent from Table I that when h_1 is (+) there are correlations between the charges of h_1 and h_2 in the data over and above the "kinematic" correlations predicted by the UMC. This can be seen by comparing the ratios (++)/(+-) in the two cases. We note that the (++)/(+-) ratio in the data falls between the UMC and the FF2 prediction, indicating that the correlations assumed by FF2 are too strong. When h_1 is negative, both the UMC and FF2 agree fairly well with the data. This may indicate that in such events information about the parent quark charge has been badly diluted. For this reason we will refer to h_1 = (+) events as "Class-A" and h_1 = (-) events as "Class-B", and subsequently study the two classes separately.

Another longitudinal variable which is useful in the study of fragmenting quarks is the rapdiity of a particle in the quark's rest frame. We define[14] this as $Y_q = Y_{lab} - \ln(W^2/m^2)$ where $Y_{lab} = .5 \ln((E+p_\parallel)/(E-p_\parallel))$ for each particle and m is the proton mass. In Fig. 7 we give the distribution of charged hadrons vs. Y_q, along with the distribution of net hadronic charge h^+-h^-. The sum h^++h^-

is the average rapidity density of positive-plus-negative tracks, whereas h^+-h^- is the difference in the number of positive and negative tracks at each rapidity value. Naively one expects to find the quark's quantum numbers carried in the hadrons which have rapidity within one or two units of the quark. Thus for a u-quark one might hope to see a bump of net hadronic charge = +2/3 (out of the total of +2 per event) concentrated near $Y_q = 0$. Instead one sees a smooth rise and plateau in the h^+-h^- which closely parallels h^++h^-. It may be that at much higher energies such charge localization effects will become apparent, but we see no evidence for them at present.

Theoretically[8,17] one expects the total rapidity "plateau" to be of width $\ln(W^2/m^2)$, with the quark (current) plateau of width $\ln(Q^2/m^2)$ and the diquark (target) plateau of width $\ln(W^2/Q^2)$. Hence, making the selection $Q^2 > 8$ GeV^2 should separate the target fragments from the current fragments by about two units of rapidity. The shape of the current "plateau" for such a Q^2 selection is shown in Fig. 8b and its height is seen to be quite comparable with that of the target fragmentation region in Fig. 8a. There is no a priori reason why the two regions should have the same rapidity density but apparently they do, at least to an accuracy of about 10%. This result, as well as the Q^2 independence in Fig. 2, agrees with the "correspondence" ideas of Bjorken and Kogut[8], but may be in conflict with some "widely accepted concepts" as discussed by Sivers.[27]

We now examine the h_1 vs. h_2 charge correlations as a function of Y_q where h_1 and h_2 are the charged hadrons with the largest and next largest values of Y_q. (This choice of h_1 and h_2 is practically

equivalent to "fastest" and "second fastest" used earlier.) In Fig. 9 we plot the distribution of the charge of h_2 for Class-A ($h_1 = (+)$) and Class-B ($h_1 = (-)$) events. For Class-A events the UMC assigns a considerable portion (+.34) of the remaining +1.0 of charge per event to the second hadron h_2, whereas the data give only (+.19±.04) to h_2. The FF2 prediction, on the other hand, gives too much negative charge to h_2. For Class-B events the UMC and FF2 results are in somewhat better agreement with the data. The conclusions are similar to those from Table I, namely for Class-A events there is a correlation of the charge of h_2 in the data which is stronger (more negative) than the "uncorrelated" UMC prediction, but not as strong as predicted by FF2. Presumably one could reproduce the data better by putting resonances and/or clusters into the Monte Carlo calculation. The present UMC calculation was designed specifically to take into account only direct π and K production with uncorrelated charges.

As mentioned earlier the kinematic charge correlations present in the UMC decrease with increasing W due to the increase of multiplicity. This can be seen in Fig. 10 where we have used W = 5, 50 and 250 GeV in calculating the UMC prediction for the charge of h_2. To produce W = 50 GeV on a stationary target requires a minimum neutrino energy of 1300 GeV so it may be impractical to eliminate the low-multiplicity kinematic charge correlation effects by going to higher energies. On the other hand, the Class-A events show a significant departure from the UMC (Fig. 9) which clearly establishes the presence of charge correlations at our present energy. These are in the general direction of, although not as strong as, those predicted by a particular model (FF2) of fragmenting quarks.

V Transverse Momentum Properties

So far we have suppressed or integrated over the transverse momentum P_T of the produced hadrons relative to the overall hadronic (virtual W^+ exchange) direction. Based on asymptotic freedom, several authors[18] have concluded that $\langle P_T^2 \rangle$ should be an increasing function of Q^2 and Z (or X_F) due to internal quark-parton momentum in the proton.

If we use all tracks the overall $d\sigma/dP_T^2$ is fairly well described by the function $\exp(-bm_T)$, $m_T = (P_T^2 + \mu^2)^{1/2}$, in which $b = 6\ (\mathrm{GeV/c})^{-1}$, and μ is the particle rest mass. The tracks in the UMC events were generated with this dependence and a factorizing flat rapidity function (see Appendix C). The UMC events, after passing our various cuts and reconstruction procedures, give rise to the curves shown in Fig. 11 for various slices of $X_F > 0$. We note, first of all, that the generated curves agree fairly well with the data, indicating that gross features of the uncut original data are also reasonably well described by the above simple generating function.

We also note in Fig. 11 a definite flattening of the P_T dependence as X_F increases. This manifests itself as an increase of $\langle P_T^2 \rangle$ with X_F as shown in Fig. 12a. The marked increase of $\langle P_T^2 \rangle$ with X_F appears similar to the "seagull effect" long known from experiments with hadro-produced hadrons.[19] The seagull effect arises from a production function $d^2\sigma/dP_T^2dY$ which is approximately independent of c.m. rapidity Y. Hence, it is a property of "longitudinal phase space" in which $d^2\sigma \propto F(P_T)\, dP_T^2 dY$. The reason for this is described in more detail in Appendix D. The UMC calculation uses this type of generating function and agrees quite well with the

data of Fig. 12a. Since the data do not show any effect beyond the UMC calculation they do not appear to tell us anything about quark-parton transverse momentum inside the proton. This is emphasized further if we plot (Fig. 12b) the $\langle P_T^2 \rangle$ vs. Y_q, where we note simply a smooth decrease consistent with the phase space boundary for $Y_q > 0$. Data similar to ours on $\langle P_T^2 \rangle$ vs. X_F have been used[20] to extract a value of $\langle k_T \rangle = .9$ GeV/c for the average internal quark-parton transverse momentum, but from the above discussion we believe this to be misleading and therefore do not attempt such a calculation.

Next we look for a Q^2 dependence of $\langle P_T^2 \rangle$ which could arise from a Q^2 dependence of the internal transverse momentum of the struck quark, according to asymptotic freedom ideas.[18] We expect such an effect to show up in those hadrons which are most directly correlated kinematically to the parent fragmenting quark. For this reason we choose Class-A events only (h_1 is (+)) and plot the $\langle P_T^2 \rangle$ of h_1 for those tracks with $Z > .3$. This is shown in Fig. 13, which does indeed indicate a Q^2 dependence; although the effect is practically accounted for by a similar rise in the UMC calculation. There is no explicit Q^2 dependence in the UMC model; the rise is due to our reconstruction procedure and cuts. If we use the UMC calculation as a base line and add to it a form linear in Q^2 we find $\langle P_T^2 \rangle$ = UMC + .003 Q^2 (dashed curve). The slope $d\langle P_T^2 \rangle / dQ^2 = .003 \pm .003$ is not in good agreement with .01 as estimated by Politzer[21] for $Z = .5$ and $Q^2 = 10$ GeV^2. The most we can say is that there appears to be a trend in the data in the direction of the expected effect.

A further inspection of the effect shown in Fig. 13 indicates that the growth of $\langle P_T^2 \rangle$ with Q^2 for these high Z tracks is entirely

due to the component of their $\vec{P}_T$ which is in the ν-μ scattering plane $P_T(in)$. The component perpendicular to the plane, $P_T(out)$, shows no Q^2 dependence (Fig. 14). The $P_T(out)$ component is the one that we measure directly, whereas $P_T(in)$ depends on the reconstruction procedure for each event. (The error in reconstructing $P_T(in)$ for tracks used in Fig. 14 is typically $\pm$ .1 GeV/c). The only suggested departure of the data from the calculation is $< |P_T(in)| >$ for events in the two highest Q^2 bins, and that is not very significant, particularly since the absolute level of the UMC lines is somewhat arbitrary.

VI Azimuthal Dependence

We examine the azimuthal dependence of the hadrons in the usual Gottfried-Jackson coordinate system in which the $\hat{z}$ axis is along the total hadron ($\vec{Q}$) direction and the $\hat{y}$ axis is perpendicular to the ν-μ plane in the direction $\vec{\nu} \times \vec{\mu}$. The azimuthal angle φ is measured from the $\hat{x} = \hat{y} \times \hat{z}$ axis, with $\tan \varphi = |P_T(out)|/P_T(in)$. Our typical error in reconstructing φ for hi-Z hadrons is $\pm 7°$ (see Appendix B).

It has been conjectured[22] that the φ distribution in deep inelastic μ-p scattering will be affected by the radiation of hard gluons from the struck quark-parton. In Fig. 15 we show the distribution in φ for that subsample of hadrons (same as in Figs. 13, 14) that we believe to be most nearly associated with the parent quark. The φ distribution for high Q^2 is peaked near $\varphi = 0$ or 180° in a manner which may not be entirely accounted for in the UMC calculation, although the departure from the UMC is not large. Recently Cohn[28] has emphasized that one expects an azimuthal dependence in the naive parton model even without gluon effects, and hence the interpretation of φ distributions may be quite complicated.

VII Summary

We have examined the details of the hadron "jet" made by high energy neutrino-proton charged current interactions. The production of high-Z hadrons is approximately independent of Q^2 and W for $W > 4$ GeV and $Q^2 < 64$ GeV^2, in agreement with the basic assumptions of the quark fragmentation model. After making the selection $Q^2 > 8$ GeV^2 to separate the current and target fragmentation regions, the heights of the rapidity plateaux in the two regions are found to be comparable (Fig. 8).

We have made several comparisons of the data with the fragmentation model of Field and Feynman (FF2) and with an uncorrelated longitudinal phase space model (UMC). The inclusive distributions of $h^{\pm}$ vs. longitudinal variables, such as X_F, are well represented by both models, as are the distributions of the fastest h^+ and h^- in each event (Fig. 6). The correlations, in a given event, between the charge of the fastest (h_1) and second fastest (h_2) hadrons are not reproduced by the UMC and therefore are stronger than "kinematic" in events where h_1 is (+). The FF2 predictions for these same correlations appear to be too strong (Fig. 9).

Turning to transverse variables, there is a sizeable rise of $\langle P_T^2 \rangle$ with Feynman X, but this is well accounted for by the UMC model (Fig. 12) and we do not, therefore, use it to measure the proton's internal quark-parton momentum. For events in which h_1 is (+) and $Z_1 > .3$, we find, after correcting for the rise in the UMC calculation, only slight evidence for an additional rise in $\langle P_T^2 \rangle$ of h_1 vs. Q^2; with the linear form $d\langle P_T^2 \rangle/dQ^2 = .003 \pm .003$

giving a reasonable fit up to $Q^2 = 64$ GeV^2. This rise is associated with the in-plane component of $\vec{P}_T$. The azimuthal angle of this same selected sample of hadrons, when an additional high-Q^2 selection is made, shows, at most, a mild anisotropy (Fig. 15).

We are indebted to many staff persons at Fermi National Accelerator Laboratory for contributions in the taking of these data. We have benefitted particularly from conversations with J.D. Bjorken, R.N. Cahn, S.D. Ellis, R.D. Field, G.L. Kane, and H.D. Politzer.

This work was supported in part by the U.S. Department of Energy and the National Science Foundation.

Table I

Charge correlations of the fastest and 2nd fastest charged hadrons. A (+) or (-) sign signifies the charge of a hadron with $Z_R > .1$. "None" signifies that Z_R is less than .1 . Numbers in table are percent of events.

h_1	h_2	FF2	Data	UMC
+	+	14.2	26.±2.	38.
+	-	20.1	24.±2.	20.
+	none	26.2	20.±2.	12.
+	any	60.5	70.±4.	70.
-	+	16.2	21.±2.	23.
-	-	4.4	3.0±.6	3.3
-	none	9.4	2.4±.5	3.0
-	any	30.0	26.±2	29.
none	none	9.5	3.8±.7	1.0

Appendix A: Muon Selection and Cut Procedures

In the present paper we make use of a kinematic method to select the μ^- in the neutrino charged-current (CC) events. We do not make direct use of the External Muon Identifier (EMI)[25] for two reasons. Although for the first exposure ($\sim$ 25% of the data) the EMI was quite efficient, its efficiency was lower in the remainder of the data due to the significantly higher neutrino flux and concomitant background. Secondly, we have found a kinematic selection method which our Monte Carlo calculations indicate is highly accurate in selecting the μ^- for the data sample that we use in this paper.

The kinematic method selects as the μ^- the negative track with the largest value of the product $F = F_1 F_2 F_3^{-1}$. In this expression F_1 is the transverse momentum relative to the beam, F_2 is the transverse momentum relative to the direction $\vec{P}_R$ of all of the rest of the visible particles, and F_3 is the square root of the sum of the squares of the transverse momenta of the rest of the visible particles relative to their total momentum $\vec{P}_R$. In other words, the algorithm looks for a single high momentum, high transverse momentum particle balanced by a clustered jet of remaining particles.

The distribution of log F for a sample of Monte Carlo events is shown in Fig. A1. The overlap of the μ^- with the negative hadrons (h^-) is shown by the dotted curves and is seen to be quite small. The individual factors F_1, F_2, F_3^{-1} have similar double peaks with less clean separations. Of the three factors, F_3^{-1} provides the least contribution to the discrimination. The method makes the wrong muon choice in only 1.5% of the CC events. Of course, there is also a neutral-current (NC) and $\bar{\nu}$ charged-current ($\overline{\text{CC}}$) background. These are greatly reduced by the cuts we make in the data, as we describe below.

In Table AI we show what happens to the various kinds of events as we successively apply the cuts in order to purify the CC sample. The selection on ΣP_x, the total visible beam-direction momentum, does not depend on the choice of muon. The cuts, P_{TR} ($= F_2$ for the chosen muon), Φ_{VIS} and R_{xyz} depend on the muon choice, but not on the reconstruction procedure. R_{xyz} is defined by searching the positive tracks for the largest value of the product F_1^2 times total momentum, and then dividing by the corresponding product for the chosen μ^-. W, x, y depend on the reconstruction procedure (see Appendix B). The mixture of CC, NC, and $\overline{CC}$ was chosen accord-ing to the analysis of the NC/CC ratio published earlier,[26] the running conditions of which were slightly different than those under which the major part of the present data were taken. However, since our cuts virtually eliminate NC and $\overline{CC}$ background our results are insensitive to the exact amount of such. The cuts also essentially eliminate the few percent neutron and K_L° interactions present after the ΣP_x cut.

Table AI. Monte Carlo study of event survival under successive cuts. (Entries are percentage of events.)

Event Selection	Total CC Events	CC Wrong μ	NC Events	$\overline{CC}$ Events	Total Monte Carlo	Data Events	Data %
$\Sigma P_x > 10$ GeV/c	74	(3.4)	19	7.3	100	2560	100
$P_{TR} > 1$ GeV/c	65	(1.6)	4.3	1.4	71	1928	75
$\Phi_{VIS} > 60°$	64	(1.4)	2.7	1.4	68	1888	74
$W > 3$ GeV	52	(1.3)	2.4	1.2	56	1360	53
$x > .05$	47.6	(.9)	2.1	1.2	51	1242	49
$y < .90$	46.0	(.8)	1.9	.9	49	1201	46.9
$R_{xyz} < 3$	45.6	(.8)	1.9	.2	48	1189	46.4

The main features to be noted from Table AI are as follows:

(1) The final sample contains (.8/48) x 100 = 1.7% wrong-μ CC events. These are not a troublesome background (see Appendix B.)

(2) The NC background is (1.9/48) x 100 = 4% and the $\overline{CC}$ background is .2/48 x 100 = .4%. The R_{xyz} cut is particularly effective in reducing this latter source, which, if not eliminated, gives a false signal of "h^+" (really μ^+) near $Z = X_F = 1.0$.

Appendix B: Reconstruction Method

The momenta that we measure directly in this experiment are illustrated as solid lines in Fig. B1. The dot-dashed line is the incoming neutrino direction which is accurately known; however, its energy is not. The plane of the diagram is determined by the outgoing muon momentum $\vec{P}_\mu$. The vector $\vec{P}_V$ is the momentum sum of all other visible particles. (This labeling assumes we have chosen the correct muon in a neutrino charged-current event. See Appendix A). $\vec{P}_o$ represents the sum of all unseen neutral particles, and $\vec{P}_H = \vec{P}_o + \vec{P}_V$ is the total of all outgoing particles except the muon. $\vec{P}_V$ and $\vec{P}_o$ have equal and opposite components (P_{OUT}) out of the plane. Hence, P_{OUT} is measured directly from $\vec{P}_V$. We indicate here just the projections in the plane.

In order to "reconstruct" the event we must try to determine $\vec{P}_H$ as accurately as possible. Since we have a hydrogen target this then determines all of the other kinematic variables, except, of course, the individual momentum vectors that make up $\vec{P}_o$ when there is more than one unseen neutral particle.

The quantity $\vec{P}_H$ is underdetermined by one variable. We attempt to determine $\vec{P}_o$ (and thus $\vec{P}_H$) from the configuration of $\vec{P}_\mu$ and $\vec{P}_\nu$ in each event. If the square of the missing transverse momentum $(P_{OUT}^2 + P_{oz}^2)$ is less than .01 $(GeV/c)^2$ than we assume there are no missing neutrals and get a solution by putting $P_{ox} = 0$ (where x is the beam direction and z is perpendicular to the beam in the plane). This happens in about 10% of the events; in the rest of the events we must find another way to estimate P_{ox}. If the total invariant mass M_o of the missing neutrals is known, then one can solve for P_{ox} from the following kinematic equation:

$$P_{ox} = (M_o^2 + P_{OUT}^2 + P_{oz}^2 - D_o^2)/2\ D_o \qquad (B1)$$

where $D_o = E_o - P_{ox} = m - D_\mu - D_\nu$ is determined from conservation of the quantity $(E - P_x)$ summed over all particles. The evaluation of D_o requires that we identify all the visible particles in order to calculate their energy in $D_\nu = E_\nu - P_{\nu x}$. Misidentification of charged K's or protons as π's causes us to underestimate D_ν and overestimate D_o. In fact D_o is often quite small so that errors in its estimation cause large errors in P_{ox} from (B1). For this reason, and because we have no good <u>a priori</u> estimate of M_o^2, we use a modification of (B1) to obtain only a lower limit on P_{ox}:

$$P_{ox}\ (MIN) = (P_{OUT}^2 + P_{oz}^2 - D_o'^2)/2\ D_o' \qquad (B2)$$

where D_c' is determined by assigning the pion mass to all charged tracks in evaluating D_ν. (If P_{ox} (MIN) is negative we set it equal to zero at this stage).

The remainder of our method to find P_{ox} follows closely a method originally proposed by Grant[24] and described also in ref. 7. We outline it below.

(1) Determine the minimum neutrino energy estimate from the above $P_{ox}(MIN)$:

$$E_{MIN} = P_{\mu x} + P_{\nu x} + P_{ox}(MIN)$$

(2) Determine the maximum neutrino energy estimate from $E_{MAX} = C\ E_{MIN}$, where C is adjusted to give the correct average $\langle Z_G \rangle = 0$. Z_G is the "Grant variable" which is the in-plane component of $\vec{P}_\nu$ perpendicular to $\vec{P}_H$. (Shown as the dotted line on Figure B1. Z_G is defined to be negative in the configuration shown). The value we use for C in this experiment is C = 1.50.

(3) Determine Z_1 and Z_2 corresponding to E_{MIN} and E_{MAX} and then obtain Z_G from the simple average $Z_G = (Z_1 + Z_2)/2$. This value of Z_G is then used to obtain P_{ox}. At this point we put a ceiling on P_{ox} by requiring that the missing neutrals not carry off more than half of the total beam-direction momentum, i.e., if P_{ox} is greater than $(P_{\mu x} + P_{\nu x})$ we set it equal to the latter. P_{ox} is then used to reconstruct all the other variables in the event. (Note that the usual deep-inelastic variables E_ν, W, Q^2, x, y .... now follow from momentum and energy conservation in hydrogen and do not depend on hadron mass assignments. The hadron mass assignments are only used to obtain D_o' in (B2)).

Appendix B

The reconstruction method can be checked directly from the data, and the appropriate value of C determined, by comparing the Z_G distribution with the P_{OUT} distribution for any group of selected events. P_{OUT} is directly measured in each event and its distribution is shown in Fig. B2, along with the distribution of the reconstructed Z_G for C = 1.50. Increasing C will increase Z_G and C has been adjusted to give $\langle Z_G \rangle \approx 0$. (There are 145 no-missing-neutrals events which have $Z_G \approx P_{OUT} \approx 0$ and which have not been plotted in Fig. B2. The 1044 events plotted satisfy the cuts described in Fig. 1, with $3 < W < 12$ GeV.) One expects the true Z_G and P_{OUT} distributions to be identical and symmetric around zero. (We neglect possible asymmetries due to things like gluon radiation from polarized W^+ bosons, which we have otherwise been unable to detect; see Sections V and VI.)

The accuracy of the reconstruction procedure can be checked on an event-by-event basis by using Monte Carlo events generated from the UMC program described in Appendix C. Some results on the accuracy in E_ν, Q^2, W, x^{-1} and y are shown in Fig. B3 (a-c) where we have plotted the distribution of the ratios of the reconstructed value to the true value for each variable. Fig. B3 is based on 1600 Monte Carlo events which obey the same cuts as the real events of Fig. B2. The dots represent 24 events from the

sample in which the muon selection procedure yielded the wrong choice. One sees from this that these events have larger errors than the others, but that they will not introduce any appreciable additional error into the event sample. (The fractional error in E_ν is the same as that of Q^2, and similarly for x^{-1} and y, because the product $xy = Q^2/2m\ E_\nu$ is directly measured and therefore independent of the reconstruction procedure. I.e., $xy = (2\ P_\mu/m)\sin^2(\theta/2)$, where θ is the angle of the muon relative to the beam. This latter expression neglects the muon rest mass.)

Finally, we show in Fig. B3d the distribution of the angular error $\delta\theta_H$ that we make in reconstructing the direction of the total hadronic system $\hat{P}_H$ $(= \hat{Q})$ in the lab. The errors in the transverse variables $P_T(in)$ and φ for individual tracks, discussed in Sections V and VI, are primarily due to the error $\delta\theta_H$. Errors in the longitudinal variables Z, X_F, Y_q are partly due to $\delta\theta_H$ and partly due to the error in the total hadronic momentum $|\vec{P}_H|$. Typical errors for tracks with $Z > .2$ are : $\delta\varphi = \pm 7°$, $\delta P_T(in) = \pm .1$ GeV/c, $\delta Z = \delta X_F = \pm .1$, $\delta Y_q = \pm .25$.

Appendix C: Description of the Monte Carlo Calculation (UMC)

The calculation begins by generating for an event the total hadronic invariant mass W, and Q^2. It does this by picking the neutrino energy E from a distribution which agrees with what we observe (using the energy reconstruction procedure described in Appendix B). It then picks the Bjorken variable x with differential probability proportional to $(1-x)^{3.5}x^{-.2}$ and flat in y for charged-current ν events and $(1-y)^2$ for charged-current $\bar{\nu}$ and neutral current background events. Given x, y, E one uses $W^2 = m^2+2mEy(1-x)$ and $Q^2 = 2mExy$ to get W and Q^2.

Given W, the hadrons are generated in the W rest frame as follows:

(1) The recoil nucleon is chosen to be a proton or neutron with equal probability. The distribution in the nucleon's variable $x_E = 2E/W$ is chosen flat between 0 and .9 with its momentum in the backward c.m. hemisphere. This determines E of the nucleon and the remaining energy, $E_R = W - E$, and recoil momentum of the system to be used for meson production.

(2) The numbers of π^+, π^-, π° to be produced are chosen using $\langle n_- \rangle = \langle n_o \rangle = (\langle n \rangle - Q_\pi)/2$, where $\langle n \rangle$ is the average number of charged pions and Q_π is their net charge. From hadronic data[23] we take $\langle n \rangle = 1.5 + 1.2\, \ell n(E_R) + .6\, \ell n^2(E_R)$. The actual number of π^- and π° in each event are then chosen from independent Poisson distributions for n_- and n_o. (Energies, etc., are in GeV units). The number of π^+ is then chosen to conserve charge. This prescription agrees with what is known about hadro-produced hadrons, except that we do not put in the known[23] correlation between $\langle n_o \rangle$ and n_-. (This correlation is not very significant at our W values.[6])

(3) A fraction of the π^+, π^-, π° are changed to K^+, K^-, K° with only pairs of K mesons being allowed; except we occasionally change a neutron to a Λ° in order to accompany a lone K^+ or K°. The fractions are adjusted to give the correct number of K° and Λ° observed in the present data.

(4) The transverse momenta $P_\perp$ of all the hadrons are generated according to $\exp(-6m_\perp)$ where $m_\perp = \sqrt{\mu^2+P_\perp^2}$ and μ is the particle mass. This feature is also taken from hadro-produced data. The two components of $\vec{P}_\perp$ are picked using a flat azimuthal (φ) distribution. Transverse momentum is conserved by summing the components in a given direction over all N particles and then subtracting 1/Nth of the sum from each value. These conservation constraints have no effect on the output $m_\perp$ and φ distributions.

(5) The longitudinal momenta $P_\parallel$ of the produced particles are generated in the rest frame of the system of invariant mass W_R recoiling against the nucleon, already determined in step (1). The rapidity (Y) of each particle in this system is picked from a flat distribution of total width $\Delta Y = 2\ln(W_R) - .4\ln(m_\perp)$. This partially accounts for the kinematic boundary $|Y_{MAX}| \approx \ln(W_R/m_\perp)$. $P_\parallel$ is then given by $P_\parallel = m_\perp \sinh Y$. The conservation of $P_\parallel$ is determined in the overall W rest frame by subtracting from each $P_\parallel$ a fraction f_1 of that particle's energy E, where $f_1 = (\Sigma P_\parallel)/(\Sigma E)$. This procedure helps to keep the rapidity distribution flat after $P_\parallel$ conservation, since $\delta y = \delta P_\parallel / E$.

(6) Energy conservation is accomplished by multiplying each $P_{\parallel}$ by a factor f_2 such that the equation $\Sigma\sqrt{(f_2 P_{\parallel})^2+m_{\perp}^2} = W$ is satisfied. This is solved by iteration, starting with the approximation $f_2^{\circ} = W/\Sigma|P_{\parallel}|$. A solution which conserves energy to within 1 MeV is usually found in 2 to 3 iterations. If the solution does not satisfy $.5 \leq f_2 \leq 2$ it is rejected. The output rapidity distribution remains reasonably flat, with small tails, after the imposition of $P_{\parallel}$ and E conservation.

Given all the particles in the event, we transform the hadrons into the lab frame and treat them as we do in the real events. We assume 2/3 of the Λ° and 1/3 of the K° are visible and that protons are identified if their momentum is $\leq$ 1 GeV/c. The charged kaons and remaining protons are treated as if they were pions.

An appropriate mixture of charged-current, neutral-current, and $\bar{\nu}$ charged-current are generated and the mixture is passed through the same analysis program as the real events. (See Appendix A.)

APPENDIX D: The Seagull Effect

The "seagull effect" arises when one plots for individual particles their average transverse momentum $\langle P_T \rangle$ or $\langle P_T^2 \rangle$ vs. the longitudinal variable $X_F = 2P_{\parallel}/W$ in the c.m. of the hadronic system. A typical (half of a) seagull is shown in Fig. 12a for $X_F > 0$. If we let Y be the c.m. rapidity and E the c.m. energy of a particle, then $Y = \ln[(E+P_{\parallel})/m_T]$, with $m_T = (P_T^2 + \mu^2)^{1/2}$ and μ the particle mass. Because of the relation $(dY) = (dP_{\parallel})/E = W(dX_F)/2E$ one has that the curve $\langle P_T^2 \rangle_{X_F}$ vs. X_F : $\langle P_T^2 \rangle_Y$ vs. Y, where the subscript indicates the longitudinal variable that is held constant during the integration over P_T. If particles are produced according to longitudinal phase space, in which

$$d\sigma = F(P_T)\, dP_T^2 dY \tag{D1}$$

then $\langle P_T^2 \rangle_Y$ vs. Y is flat but $\langle P_T^2 \rangle_{X_F}$ vs. X_F will show the seagull effect. We show below the reason for this.

In general one writes

$$\langle P_T^2 \rangle_{X_F=C} = \int P_T^2 \left(d^2\sigma/dP_T^2 dX_F\right) dP_T^2 \Big/ \int \left(d^2\sigma/dP_T^2 dX_F\right) dP_T^2$$

Using the above definition of $d\sigma$ this becomes

$$\langle P_T^2 \rangle_{X_F=C} = \int_0^P \frac{P_T^2 F(P_T)}{E}\, dP_T^2 \Big/ \int_0^P \frac{F(P_T)}{E}\, dP_T^2 \tag{D2}$$

where E is evaluated at $X_F = C$, i.e.,

$$E = (W/2)\sqrt{C^2 + 4m_T^2/W^2}\,. \tag{D2a}$$

On the other hand, using the assumed form for $d\sigma$, one gets for constant Y:

APPENDIX D
2

$$\langle P_T^2\rangle_{Y=C'} = \int_0^{P'} P_T^2\, F(P_T)\,dP_T^2 \Big/ \int_0^{P'} F(P_T)\,dP_T^2 \qquad \text{(D3)}$$

The upper limits of these integrals are functions of W and C (C') which come from the kinematic boundary. Because of the rapid exponential fall-off of $F(P_T)$ these upper limits only have an appreciable effect when X_F or Y are near their maximum values. This is what causes the "seagull's wing" to turn over at $X_F \approx .8$ in Fig. 12a

The one place where (D2) and (D3) can be compared directly is along the line $X_F=Y=0$:

$$\langle P_T^2\rangle_{X_F=0} = \int_0^{W/2} \frac{P_T^2 F(P_T)}{m_T}\, dP_T^2 \Big/ \int_0^{W/2} \frac{F(P_T)}{m_T}\, dP_T^2 \qquad \text{(D4)}$$

or, changing variables, and assuming the upper limits are effectively infinite,

$$\langle m_T^2\rangle_{X_F=0} = \int_{\mu}^{\infty} m_T F(m_T)\,dm_T^2 \Big/ \int_{\mu}^{\infty} \frac{F(m_T)}{m_T}\, dm_T^2 \qquad \text{(D5)}$$

whereas,

$$\langle m_T^2\rangle_{Y=0} = \int_{\mu}^{\infty} m_T^2\, F(m_T)\, dm_T^2 \Big/ \int_{\mu}^{\infty} F(m_T)\, dm_T^2 \qquad \text{(D6)}$$

so that

$$\langle m_T^2\rangle_{X_F=0} = \langle m_T\rangle_{Y=0} / \langle m_T^{-1}\rangle_{Y=0} \qquad \text{(D7)}$$

We see from (D7) that, in general, $\langle m_T^2\rangle_{X_F=0} \neq \langle m_T^2\rangle_{Y=0}$, even though the two averages are computed along the same line $X_F=Y=0$ in the c.m. If we use the generating functions

$F(m_T)=\exp(-bm_T)$ with $b=6(\text{GeV/c})^{-1}$ and μ=pion mass we obtain from (D5) and (D6)

$$\langle P_T^2\rangle_{Y=0} = .19\ (\text{GeV/c})^2 \text{ and } \langle P_T^2\rangle_{X_F=0} = .10(\text{GeV/c})^2.$$

These are in good agreement with what we observe in the data.

The shape of the seagull comes from the growth of $\langle P_T^2\rangle_{X_F=C}$ with increasing X_F, as seen in Fig. 12a. This can be understood from eqns. (D2) and (D2a) which predict that $\langle P_T^2\rangle_{X_F=C}$ approaches $\langle P_T^2\rangle_{Y=0}$ if $X_F \gg 4m_T^2/W^2$ all during the P_T integration. The fact that, experimentally, $\langle P_T^2\rangle_{X_F=C}$ becomes <u>larger</u> than $\langle P_T^2\rangle_{Y=0} = .19$ is due to some actual diminuation with increasing Y of the experimental $d^2\sigma/dP_T^2\,dY$. That is to say, suppose instead of (D1) we have

$$d\sigma = F(P_T, Y)\ dP_T^2 dY \qquad (D1')$$

with F being a decreasing function of Y. Then holding $X_F=C\neq 0$ during the P_T integration gives decreasing Y with increasing P_T and prevents F from falling as fast as it does at $X_F=Y=0$. (The decrease of Y with P_T at fixed X_F can be seen from the relation $X_F=(2m_T/W)\sinh Y$).

The data do show a decrease of F with Y at fixed P_T and the same is true of the output UMC calculation, even though in the input we assumed no Y dependence. (The generated Y dependence comes from our application of energy and momentum conservations constraints.) Hence, both the data and the UMC calculations of $\langle P_T^2\rangle$ vs. X_F show a seagull effect that rises above the central value $\langle P_T^2\rangle_{Y=0}$ and then drops to zero, as it must, near $X_F= \pm 1$.

REFERENCES

1. R.D. Field and R.P. Feynman, Phys. Rev. D15, 2590 (1977)
2. J.W. Chapman et al., Phys. Rev. D14, 5 (1976); Phys. Rev. Letters 36, 124 (1976).
3. R.P. Feynman, "Photon-Hadron Interactions," Frontiers in Physics series, David Pines, Editor, Published by W.A. Benjamin, Inc., Reading, Mass. (1972).
4. It is important to eliminate $\overline{CC}$ events since they produce high momentum μ^+, which, if treated as hadrons, will dominate the high X_F region.
5. A Study of the Reaction $\nu p \to \mu^- p \pi^+$, present authors, (to be published).
6. C. del Papa et al., Phys. Rev. D13, 2934 (1976); K. Bunnel et al., SLAC-PUB-2061, USC #76-052 (Dec. 1977).
7. S.J. Barish et al., Carnegie-Mellon University, Report No. COO-3066-61 (unpublished).
8. J.D. Bjorken, Phys. Rev. D7, 282 (1973), and "Hadron Final States in Deep Inelastic Processes", SLAC-PUB-1756 (May 1976); J.D. Bjorken and J. Kogut, Phys. Rev. D8, 1341 (1973).
9. J.F. Martin et al., Phys. Rev. Letters 40, 283 (1978).
10. C.J. Bebek et al., Phys. Rev. Letters 34, 1115 (1975).
11. D functions from lower energy ν and $\bar{\nu}$ interactions in a heavy liquid bubble chamber, without W cuts, have been published earlier. M. Hagenauer, Proc. of the XVII International Conf. on High Energy Physics, London (1974).
12. M. Derrick et al., Phys. Rev. 17 1 (1978).
13. L.S. Osborne, Phys. Letters 63B, 456 (1976).
14. The definition of the quark rest frame is not precise. Operationally one assumesthe total width of the pion rapidity region is given by $\ln(W^2/M^2)$ with M $\sim$ 1 GeV/c^2 in hadron collisions, and that the low energy end lines up in the lab, or

target rest frame. (The accuracy of this, and whether it depends on Q^2, can be tested with more data.) The definition $Y_q = Y_{lab} - \ln (W^2/M^2)$ then simply lines up the high energy end of the pion rapidity region for events with different W values. (In practice we M = m = .938 GeV.)

15. The D functions from Ref. 1 and 13 are shown plotted on on earlier sample of our data in Proc. of the XIIth Recontre de Moriond, p. 370, Flaine, France (1977), Ed. by J. Tran Than Van.

16. R.D. Field and R.P. Feynman, A Parameterization of the Properties of Quark Jets, Phys. Rev. (to be published).

17. R.N Cahn and E.W. Colglazier, Phys. Rev. D8, 3019 (1973) and Phys. Rev. D9, 2658 (1974).

18. Recent discussions of this, and earlier references, can be found in the following preprints: E.G. Floratos, Ref. TH. 2261-CERN (1976); J.C. Polkinghorne, Ref. TH. 2333-CERN (1977); M. Gronau, Technion-PH-77-73 (Haifa 1977); H.D. Politzer, HUTP-77/A038 (Harvard, 1977) and CALT-68-628 (Cal Tech 1978); M. Gronau and Y. Zarmi (Ref. 20).

19. For a seagull plot from 100 GeV pp collisions see C. Bromberg et al., Nucl. Phys. B107, 82 (1976), and earlier references therein.

20. M. Gronau and Y. Zarmi, How to Measure the Transverse Momentum of Partons, Phys. Rev. (to be published).

21. H.D. Politzer, Ref. 18.

22. H. Georgi and H.D. Politzer, Phys. Rev. Letters 40, 3 (1978); H. Georgi, "The Use and Misuse of the Parton Model", Preprint HUTP-78/A003, Harvard University (1978).

23. J. Whitmore, Physics Reports 10, 274 (1974). An $\langle n_- \rangle$ vs. n_- correlation has also been observed in $\bar{\nu}p$ interactions. (see ref. 12).

24. A. Grant, Nucl Instr. and Meth. 127, 355 (1975)

25. R.J. Cence et al., Nucl. Instr. and Meth. 138, 245 (1976)

26. F.A. Harris et al., Phys. Rev. Letters 39, 437 (1977)

27. D. Sivers, Phys. Rev. D15, 1306 (1977).

28. R.N. Cahn, Azimuthal Dependence in Leptoproduction: A Simple Parton Model Calculation, University of Michigan preprint UM HE (1978).

Figure Captions

Fig. 1. Distribution of invariant mass of the hadronic system for a sample of neutrino charged-current events. See text for meaning of the cuts listed. Typical mass resolution is ±15% for the bulk of the events, which have missing neutrals (see Appendix B). The peak at the left is due to the final state $\mu^- \Delta^{++}$.

Fig. 2. Average number of charged particles in the hadronic system vs. Q^2 for various W slices taken from Fig. 1. The dashed lines represent the overall average for each W slice.

Fig. 3. The rate of production of positive and negative hadrons with $Z > .2$ as a function of W. We take the Feynman scaling (W-independent) region as $W > 4$ GeV. The curves are the result of the Monte Carlo model described in the text.

Fig. 4. The D_u^+ function vs. Feynman X in the hadronic rest frame. Identified (ID) and the estimated mis-identified protons are indicated. The normalization of the UMC model is absolute and not adjusted to fit the data (see Appendix C. This is true on all Figs. except Fig. 15 where we have renormalized to the observed numbers of low-Q^2 and high-Q^2 events). In addition to the cuts on Fig. 1 the selection $W > 4$ GeV has been made in Figs. 4 through 12.

Fig. 5. (a) The (positive/negative) hadron ratio vs. X_F .
(b) The D_u^- function vs. X_F. The average number of negative tracks (integral of the graph) is indicated.

Fig. 6. (a) and (b). The distribution in Z_R of the "fastest" positive and negative tracks in each event. The dashed curves are the

predictions of Field and Feynman. Fig. 6a includes (+) tracks from events where the fastest track is negative and vice-versa for 6b.

Fig. 7. The total charged hadron rate $(h^+ + h^-)$ and net charge $(h^+ - h^-)$ per event vs. rapidity in the "quark rest frame" (see text and Ref. 14). The UMC predictions are also shown. The error bars on the open circles are the same absolute size as those on the solid circles above them.

Fig. 8. Charged hadron rate for high-Q^2 events plotted vs. lab rapidity and quark-frame rapidity. The approach to and height of the two "plateaux" are very similar.

Fig. 9. (a) Net charge of the second fastest (h_2) particle when the fastest (h_1) is negative, plotted vs. rapidity of h_2 in the quark frame. (Class B events)

(b) Same as (a) for events in which h_1 is positive. (Class A events)

The dashed curves are the predictions from Field and Feynman. The solid curves are from the UMC calculation. The average charge of the 2nd (h_2) particle (integral under the curve) is shown in each case.

Fig. 10. (a) and (b). Predictions of the UMC model for the quantities defined in Fig. 9 (a) and (b), but for various W values. In (a) one sees "kinematic" correlations present ($Q_{2ND} \neq 0$) even at W = 250 GeV.

Fig. 11. Charged hadron rate vs. transverse momentum squared for various slices of Feynman X in the positive c.m. hemisphere (current fragmentation region). Solid curves are from the UMC model.

Fig. 12. (a) Average transverse momentum squared vs. X_F for charged tracks. The seagull effect, seen here, is discussed in detail in Appendix D.

(b) Same plotted vs. rapidity in the quark frame. $X_F > 0$ corresponds roughly to $Y_q > -2$.

Fig. 13. $\langle P_T^2 \rangle$ vs. Q^2 for h_1 tracks with $Z > .3$ in events where h_1 is (+). There are 497 events (and 497 tracks) in the plot with average Z value $\langle Z \rangle = .45$. Events with 3 GeV < W < 12 GeV are used. The dashed curve is a fit to a linear function of Q^2 which has been <u>added</u> to the base-line curve (solid) calculated with the UMC model.

Fig. 14. Data from Fig. 13 is split into its components in and out of the scattering plane. (Note the broken vertical scale.) Solid curves are the UMC calculation. The Q^2 dependence in the UMC is not an input but arises from the reconstruction and cut procedures in the generated events.

Fig. 15. Azimuthal angle of tracks from Figs. 13 and 14 plotted for high- and low-Q^2 events. A track with $\varphi = 0$ would be in the scattering plane on the muon side of the total hadron momentum ($\vec{Q}_{lab}$) vector. (φ is the standard Gottfried-Jackson azimuthal angle.) The anisotropy in the UMC curves is due to our reconstruction and cut procedures.

Fig. A1. Distribution vs. log F of negative tracks in Monte Carlo events with ≥ 2 negatives. (F is the parameter used to select the muon.) The events used are pure charged-current and have the selections indicated on Fig. 1, plus W > 3 GeV made . The dashed curves show the overlap between the hadrons (h^-) and the muon.

Fig. B1. Momentum vectors used in the reconstruction procedure.

Fig. B2. Distribution of data sample vs. P_{OUT} (which we measure directly) and Z_G (which results from our reconstruction procedure). In addition to those listed, the cuts are as in Fig. 1.

Fig. B3. Errors of various quantities due to our reconstruction procedure. In a, b, c the ratio plotted is the reconstructed value divided by the true value. In d we plot the reconstructed direction of the hadronic system ($\vec{Q}$ direction) minus its true direction.

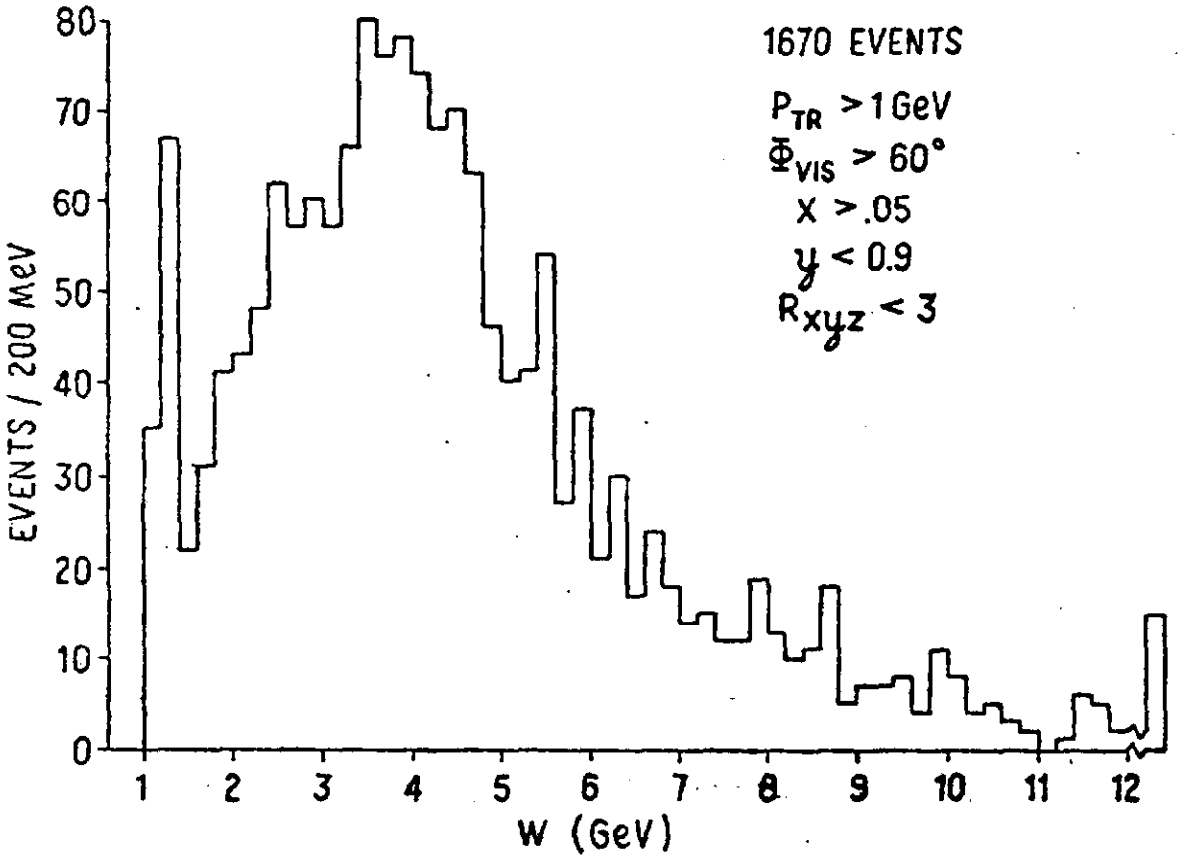
1670 EVENTS
$P_{TR} > 1$ GeV
$\Phi_{VIS} > 60°$
$x > .05$
$y < 0.9$
$R_{xyz} < 3$
EVENTS / 200 MeV
W (GeV)
0
10
20
30
40
50
60
70
80
1
2
3
4
5
6
7
8
9
10
11
12

Fig. 1

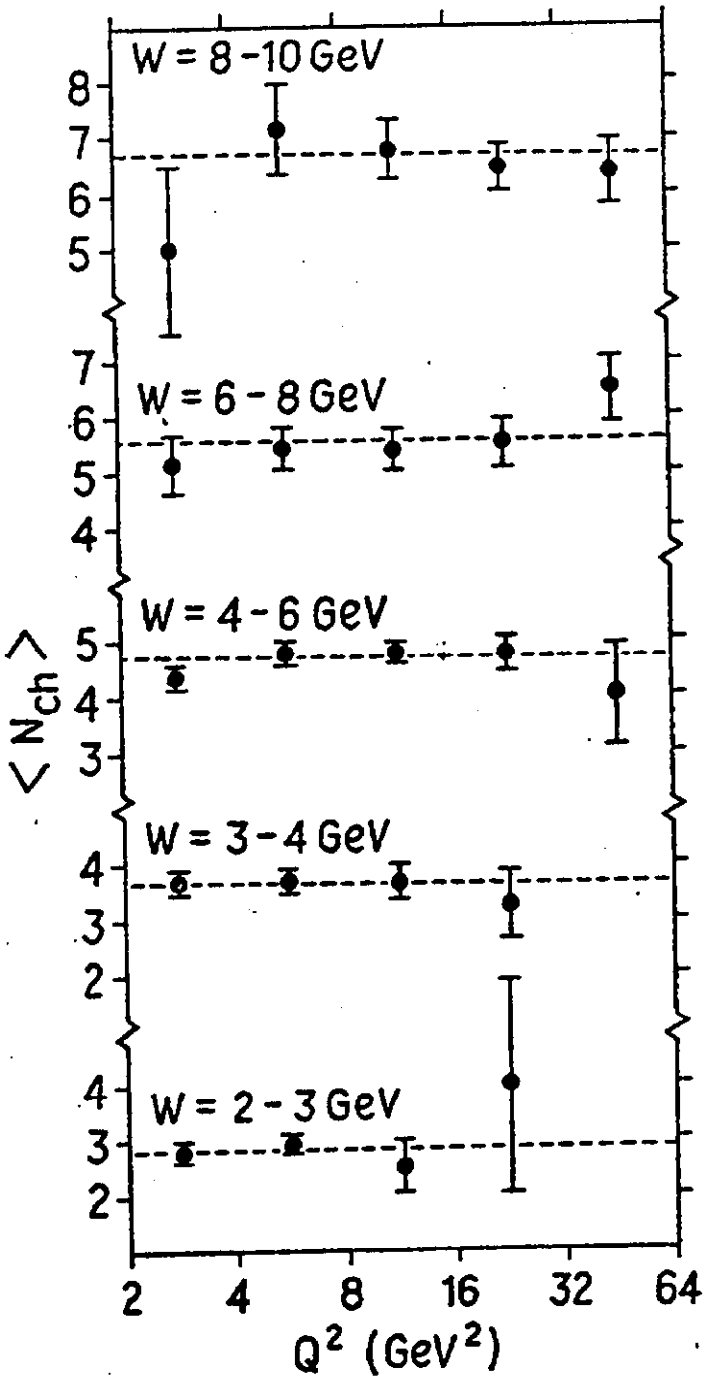

Fig. 2

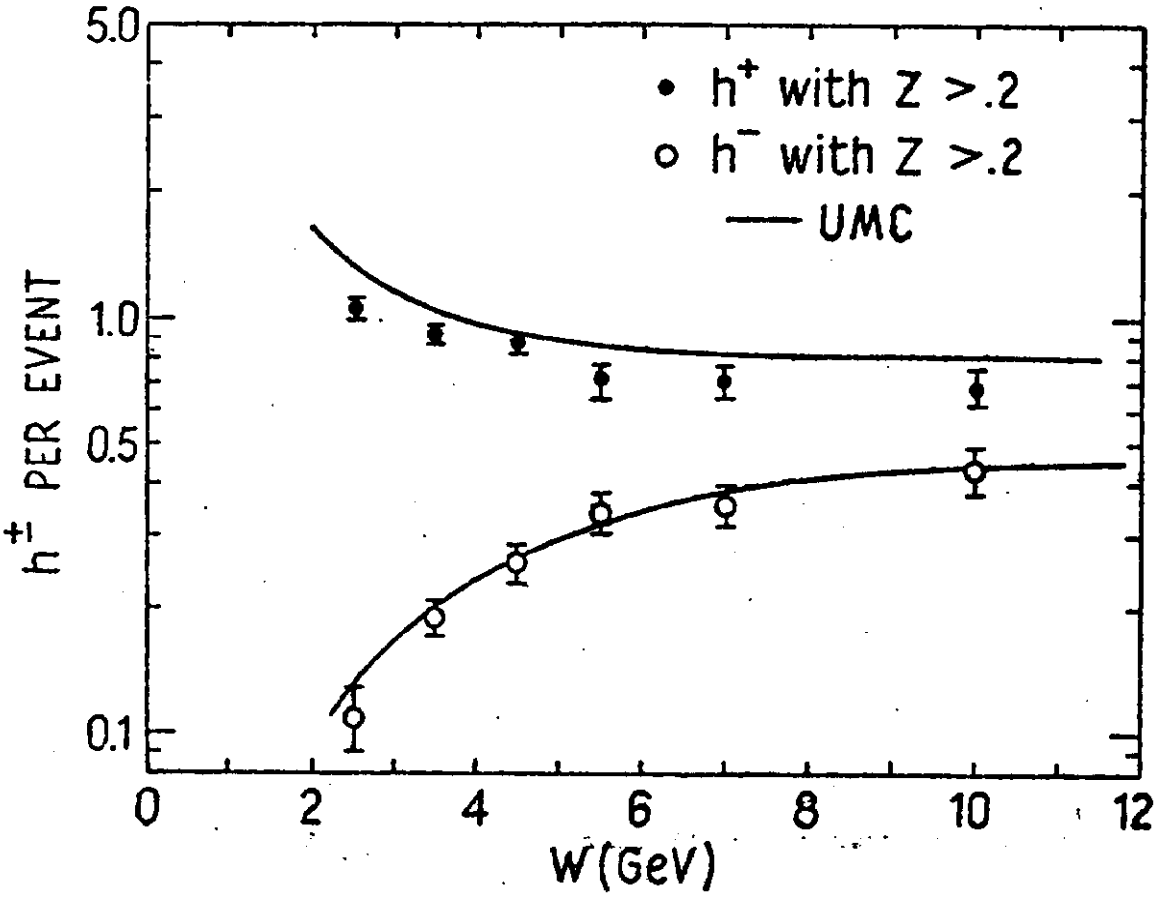

Fig. 3

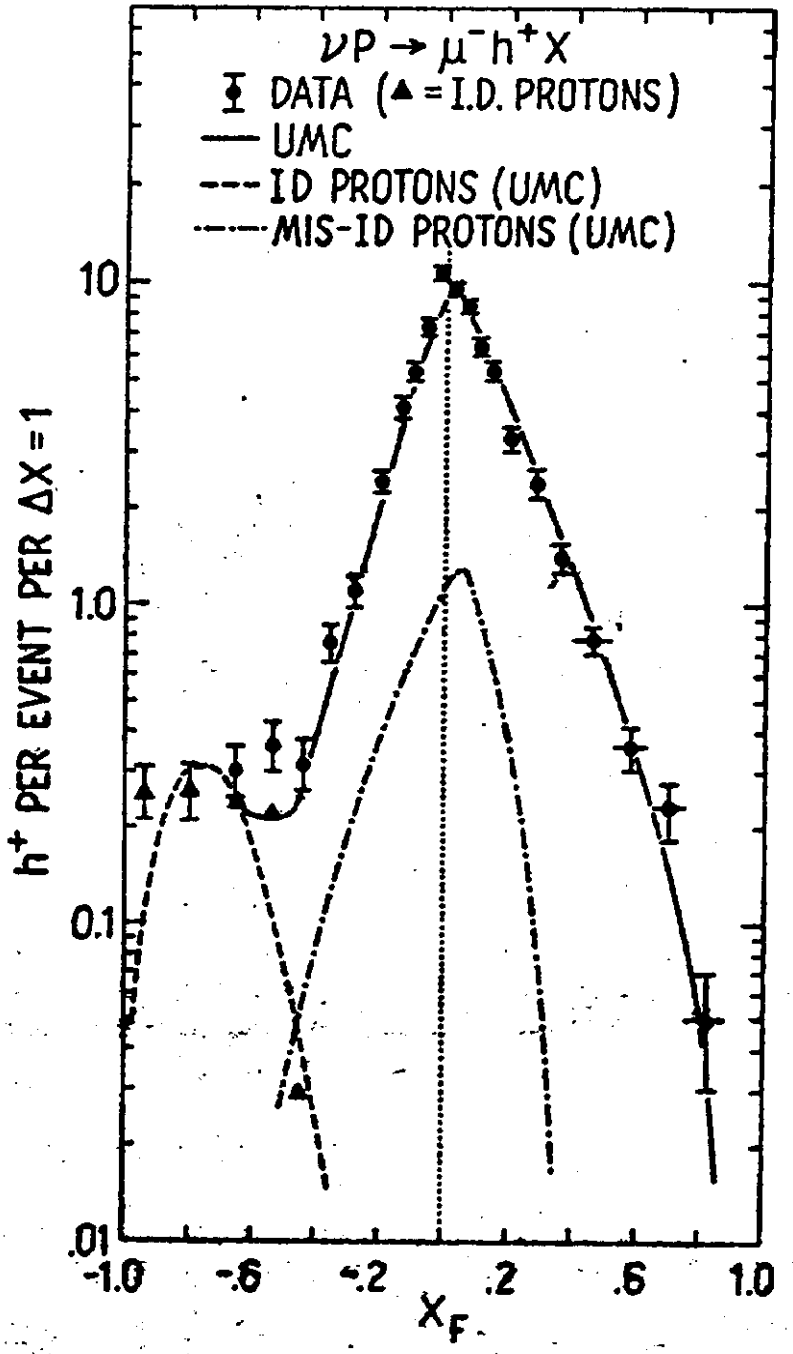
νP → μ⁻h⁺X
DATA (▲ = I.D. PROTONS)
UMC
ID PROTONS (UMC)
MIS-ID PROTONS (UMC)
h⁺ PER EVENT PER ΔX = 1
10
1.0
0.1
.01
-1.0
-.6
-.2
.2
.6
1.0
X_F

Fig. 4

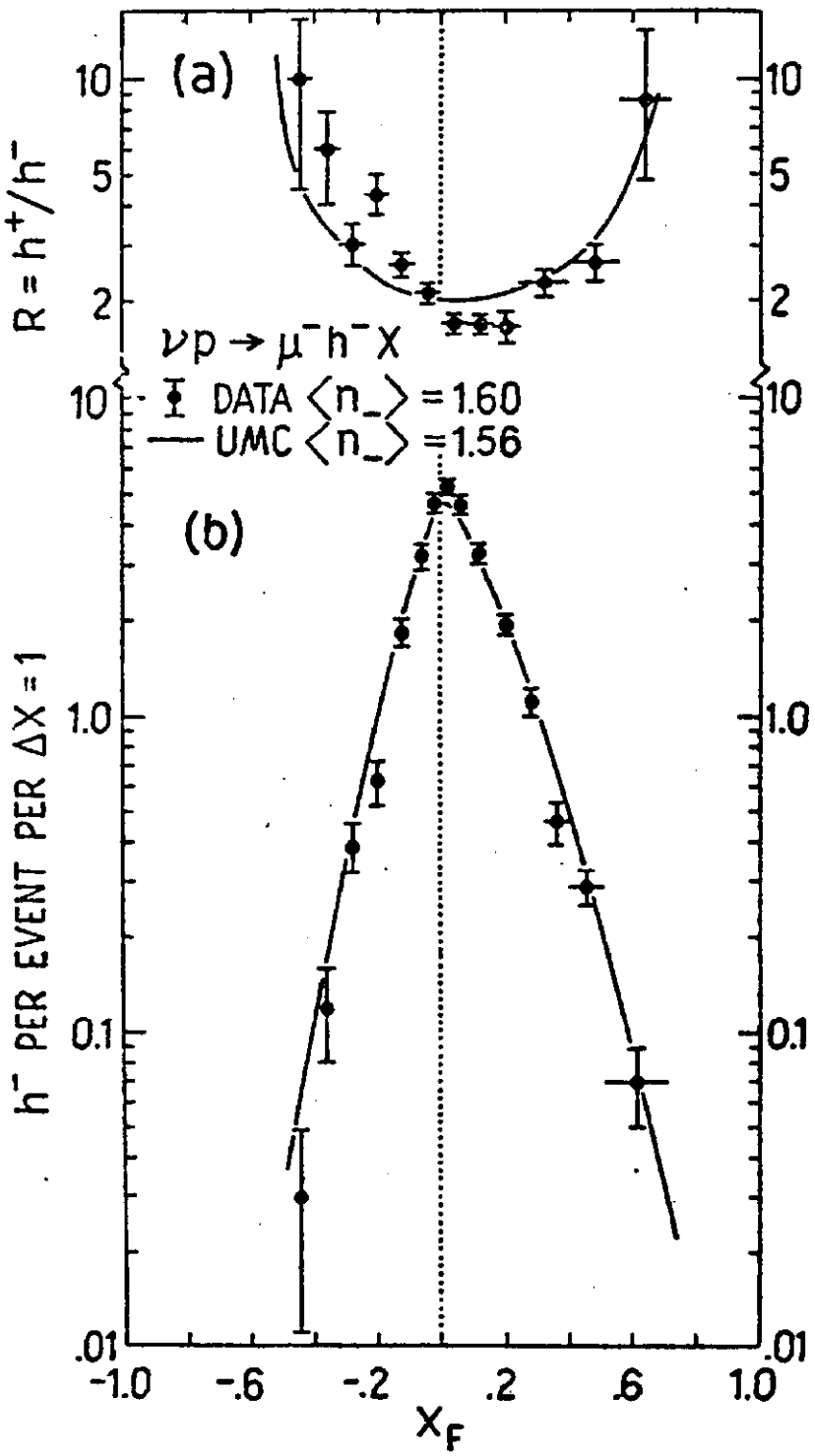
(a)
(b)
$R = h^+/h^-$
h^- PER EVENT PER $\Delta X = 1$
$\nu p \rightarrow \mu^- h^- X$
DATA $\langle n_- \rangle = 1.60$
UMC $\langle n_- \rangle = 1.56$
10
5
2
1.0
0.1
.01
-1.0
-.6
-.2
.2
.6
1.0
X_F

Fig. 5

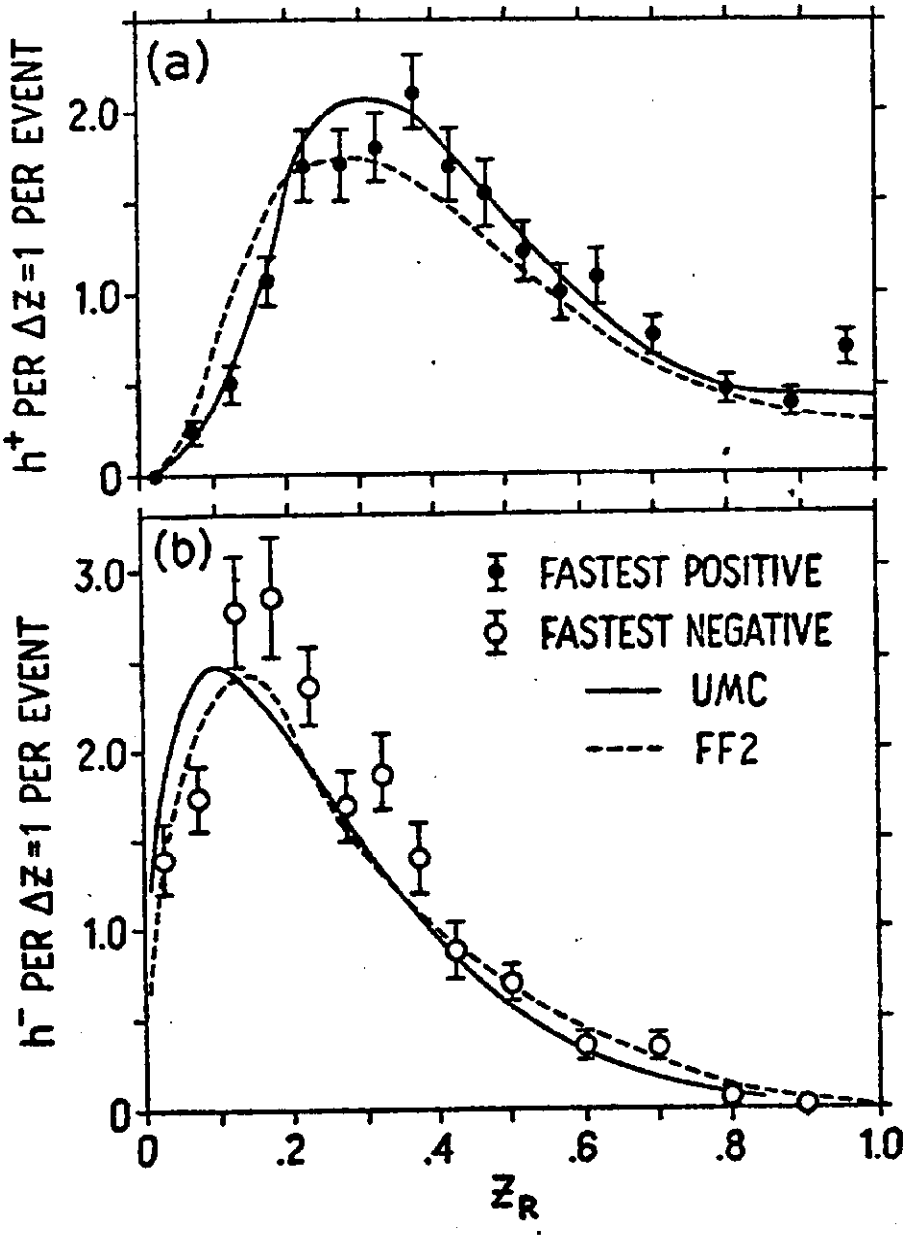
(a)
(b)
h^+ PER Δz=1 PER EVENT
h^- PER Δz=1 PER EVENT
FASTEST POSITIVE
FASTEST NEGATIVE
UMC
FF2
z_R
0
1.0
2.0
3.0
.2
.4
.6
.8

Fig. 6

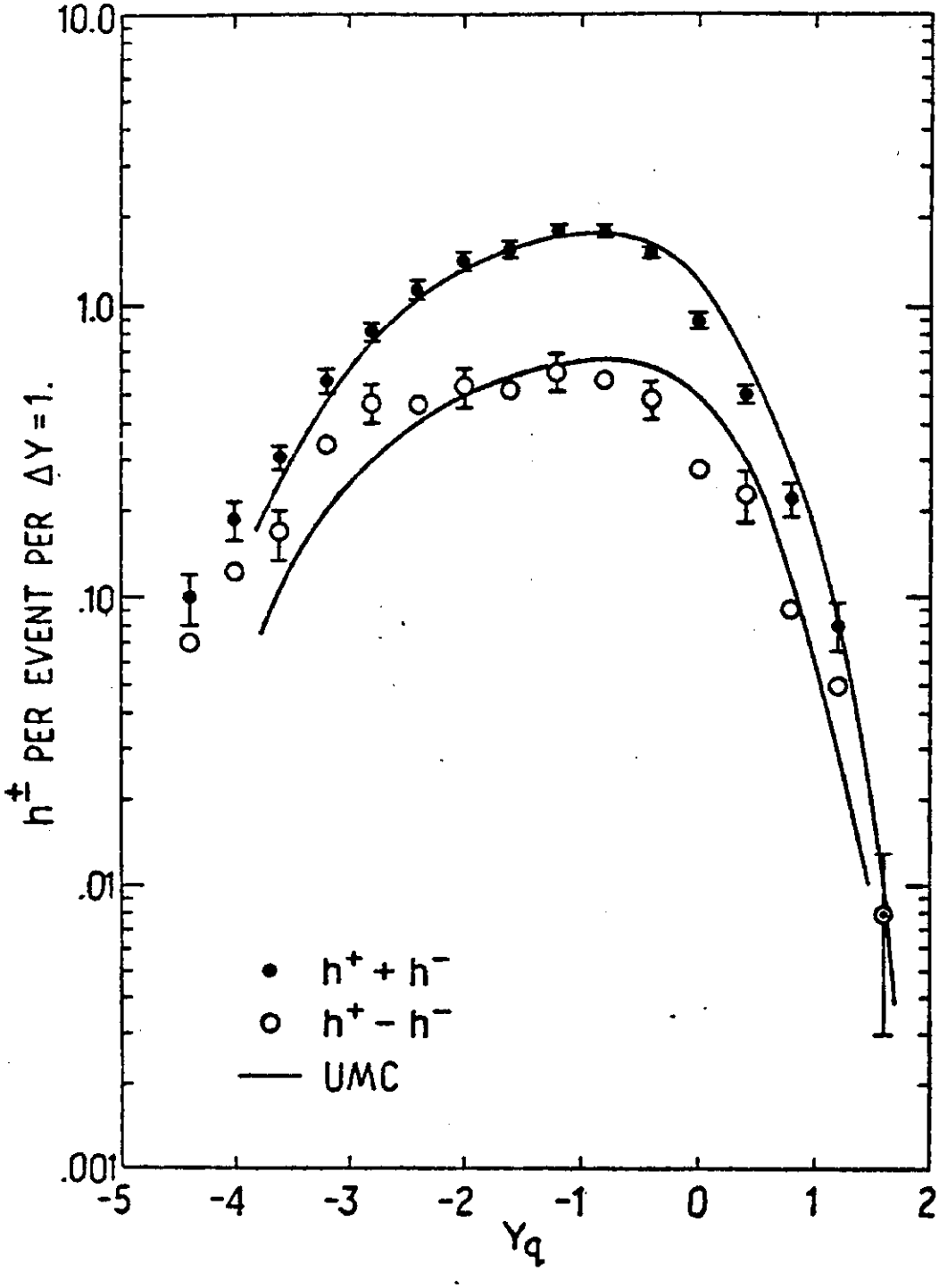
10.0
1.0
.10
.01
.001
$h^{\pm}$ PER EVENT PER $\Delta Y = 1$.
-5
-4
-3
-2
-1
0
1
2
Y_q
$h^+ + h^-$
$h^+ - h^-$
UMC

Fig. 7

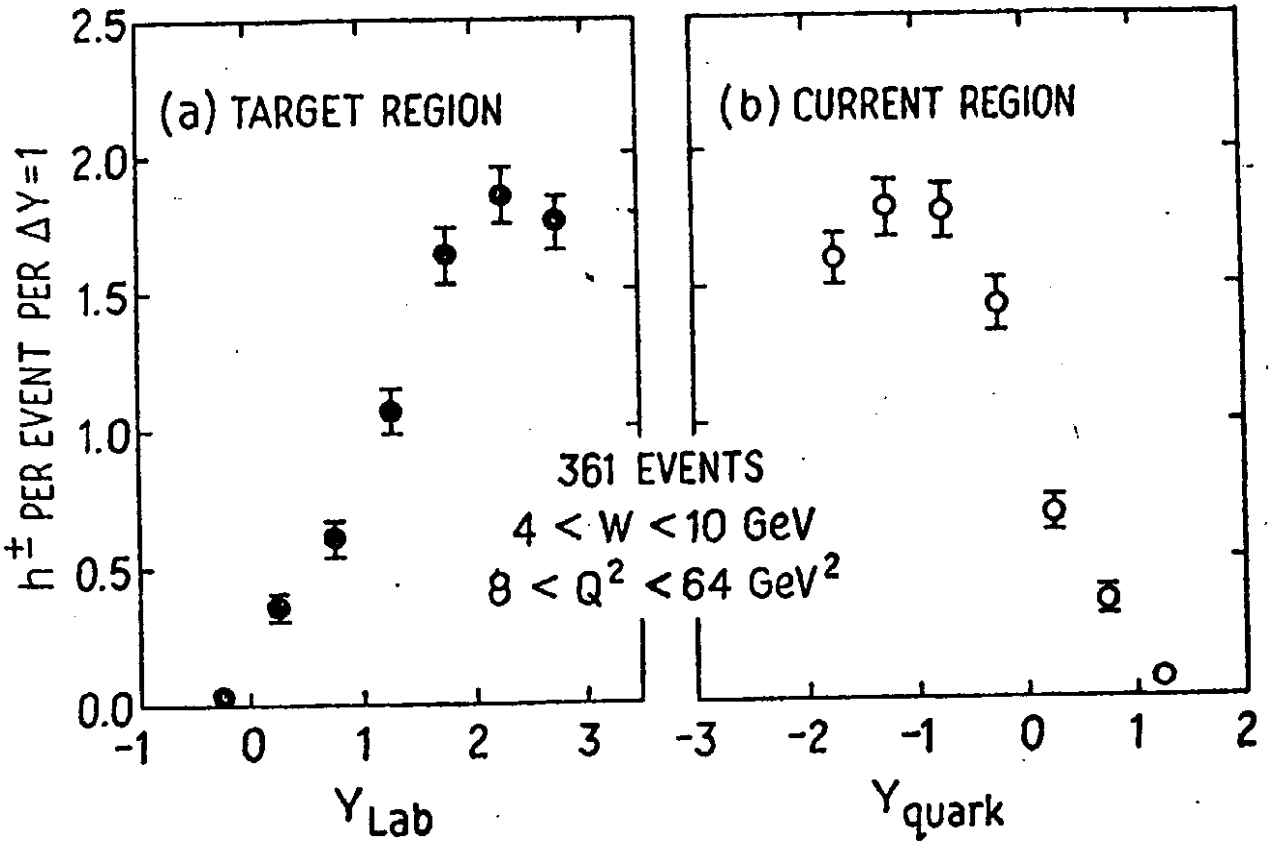
(a) TARGET REGION
(b) CURRENT REGION
361 EVENTS
4 < W < 10 GeV
8 < Q² < 64 GeV²
h± PER EVENT PER ΔY=1
Y_Lab
Y_quark
2.5
2.0
1.5
1.0
0.5
0.0
-1
0
1
2
3
-3
-2
-1
0
1
2

Fig. 8

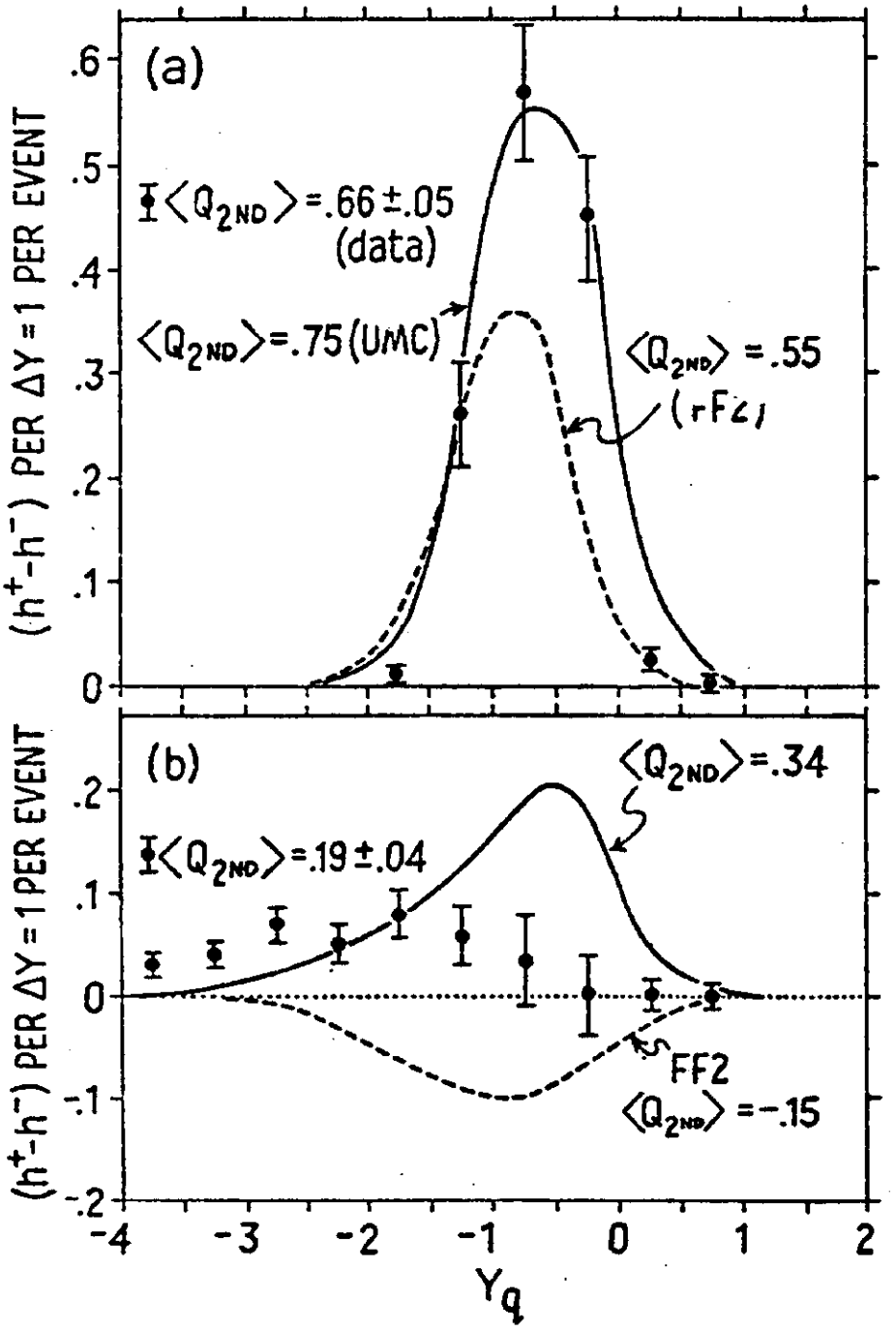
(a)
$\langle Q_{2ND} \rangle = .66 \pm .05$
(data)
$\langle Q_{2ND} \rangle = .75$ (UMC)
$\langle Q_{2ND} \rangle = .55$
(rFZ)
$(h^+ - h^-)$ PER $\Delta Y = 1$ PER EVENT
.6
.5
.4
.3
.2
.1
0
(b)
$\langle Q_{2ND} \rangle = .34$
$\langle Q_{2ND} \rangle = .19 \pm .04$
FF2
$\langle Q_{2ND} \rangle = -.15$
$(h^+ - h^-)$ PER $\Delta Y = 1$ PER EVENT
.2
.1
0
-.1
-.2
-4
-3
-2
-1
0
1
2
Y_q

Fig. 9

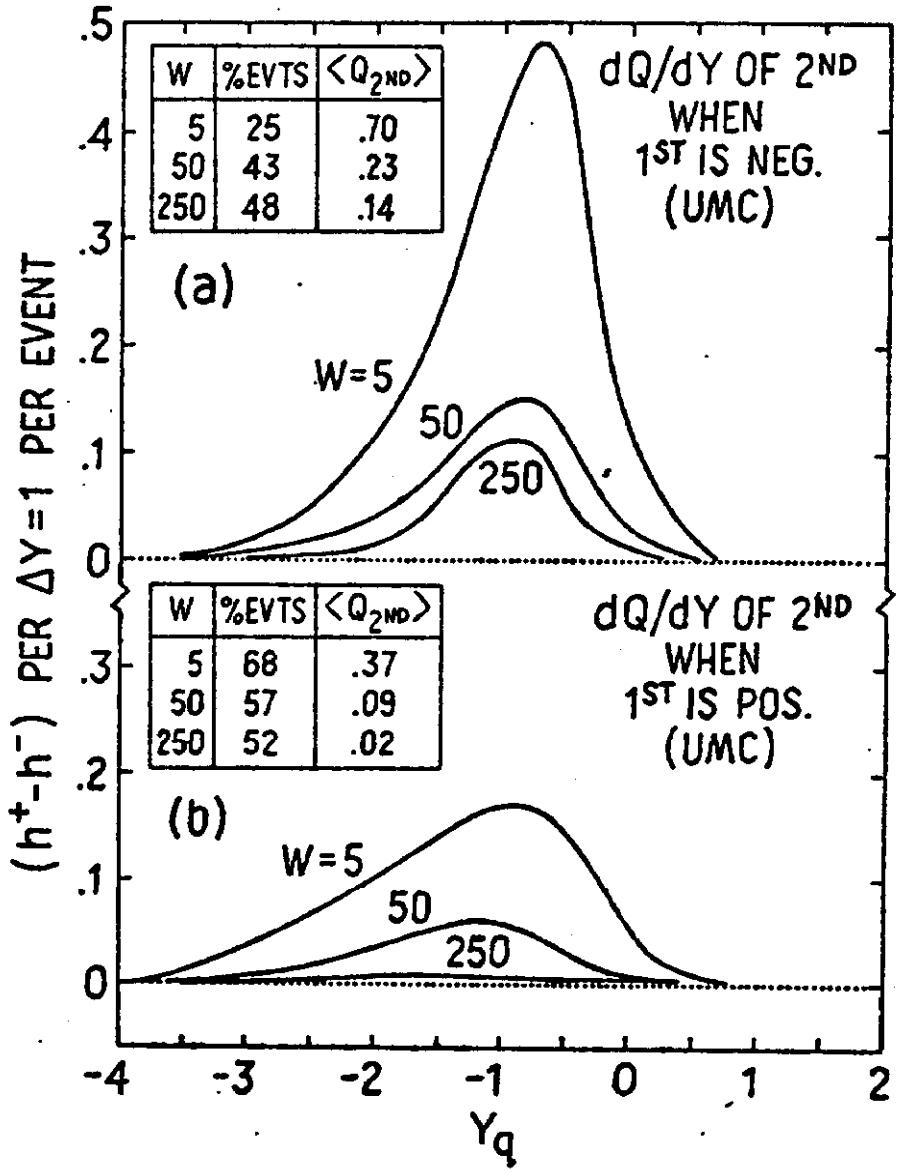
W | %EVTS | <Q2ND>
5 | 25 | .70
50 | 43 | .23
250 | 48 | .14
dQ/dY OF 2ND WHEN 1ST IS NEG. (UMC)
(a)
W=5
50
250
W | %EVTS | <Q2ND>
5 | 68 | .37
50 | 57 | .09
250 | 52 | .02
dQ/dY OF 2ND WHEN 1ST IS POS. (UMC)
(b)
W=5
50
250
(h+-h-) PER ΔY=1 PER EVENT
.5
.4
.3
.2
.1
0
.3
.2
.1
0
-4
-3
-2
-1
0
1
2
Yq

Fig. 10

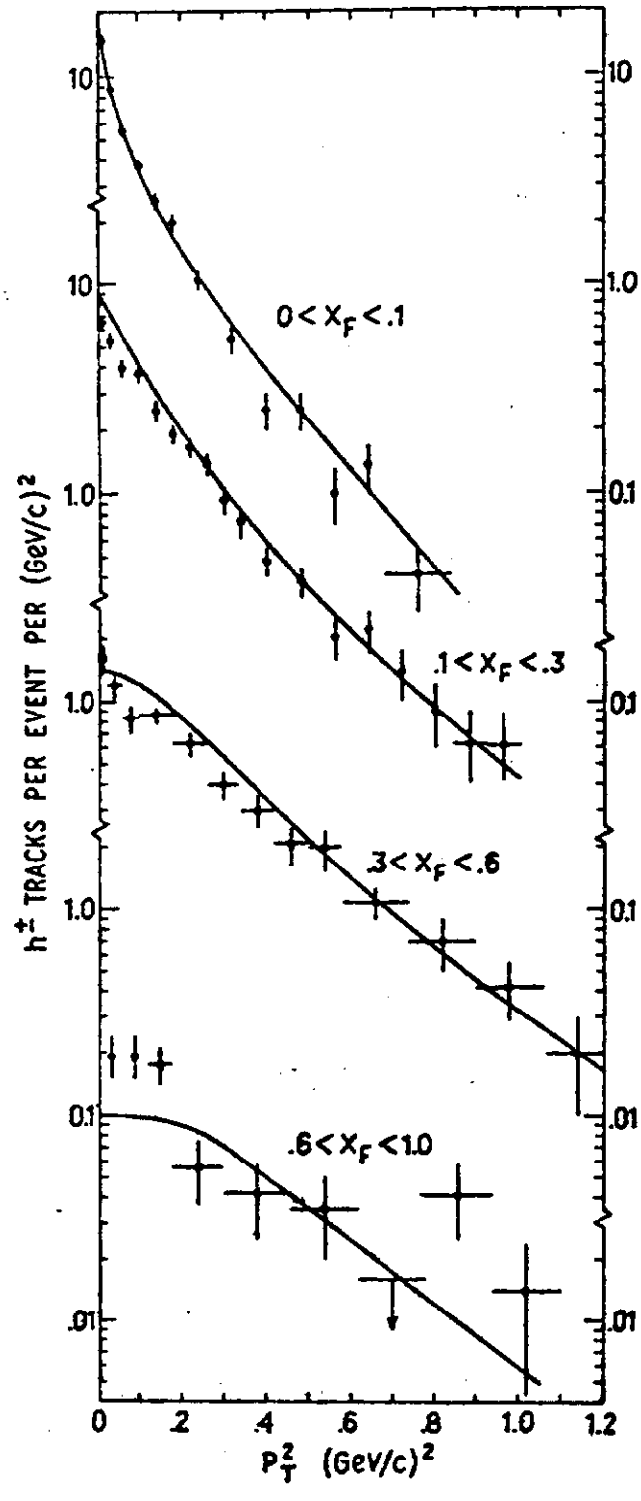
$h^{\pm}$ TRACKS PER EVENT PER (GeV/c)^2
P_T^2 (GeV/c)^2
$0 < X_F < .1$
$.1 < X_F < .3$
$.3 < X_F < .6$
$.6 < X_F < 1.0$
10
1.0
.1
.01
0
.2
.4
.6
.8
1.0
1.2

Fig. 11

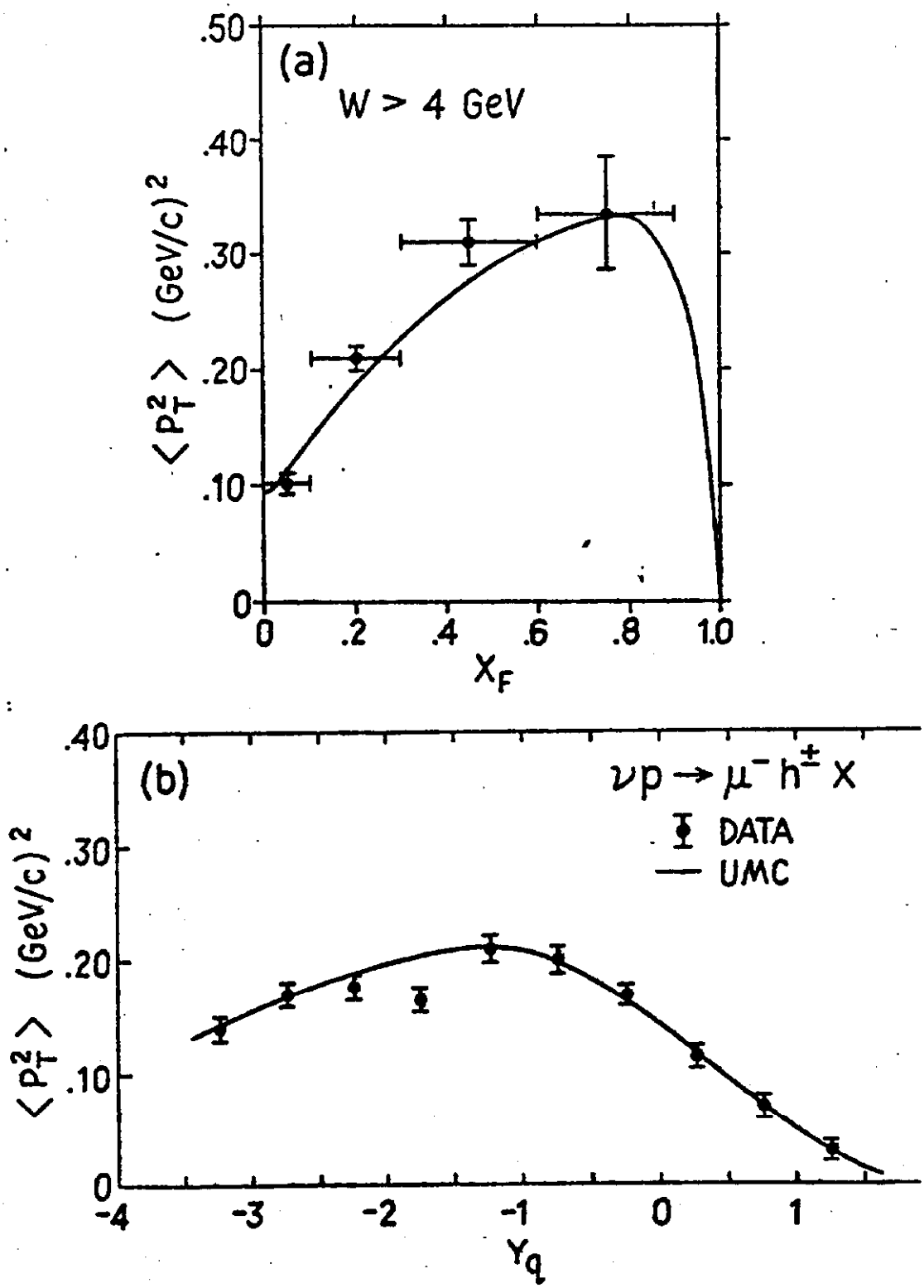
(a)
W > 4 GeV
$\langle P_T^2 \rangle$ (GeV/c)^2
X_F
(b)
$\nu p \rightarrow \mu^- h^{\pm} X$
DATA
UMC
$\langle P_T^2 \rangle$ (GeV/c)^2
Y_q

Fig. 12

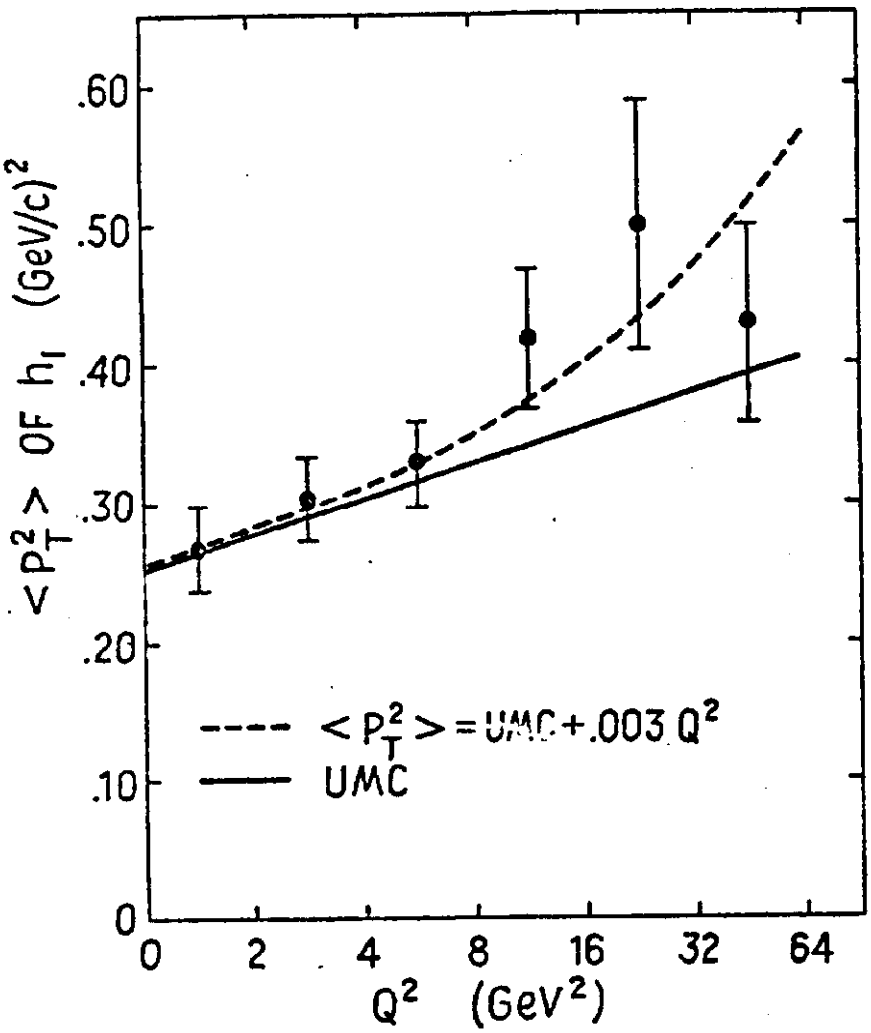
.60
.50
.40
.30
.20
.10
0
$\langle P_T^2 \rangle$ OF h_1 (GeV/c)^2
$\langle P_T^2 \rangle$ = UMC + .003 Q^2
UMC
0
2
4
8
16
32
64
Q^2 (GeV^2)

Fig. 13

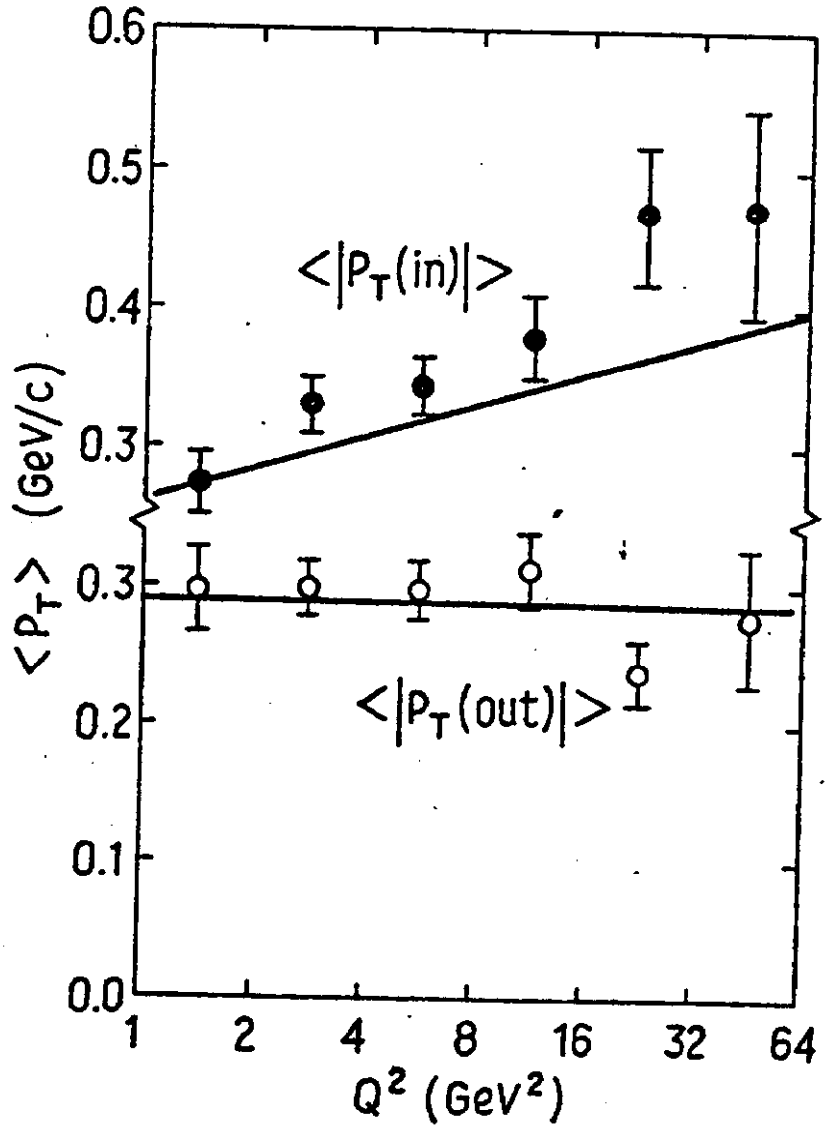
0.6
0.5
0.4
0.3
0.3
0.2
0.1
0.0
$\langle P_T \rangle$ (GeV/c)
$\langle |P_T(in)| \rangle$
$\langle |P_T(out)| \rangle$
1
2
4
8
16
32
64
Q^2 (GeV^2)

Fig. 14

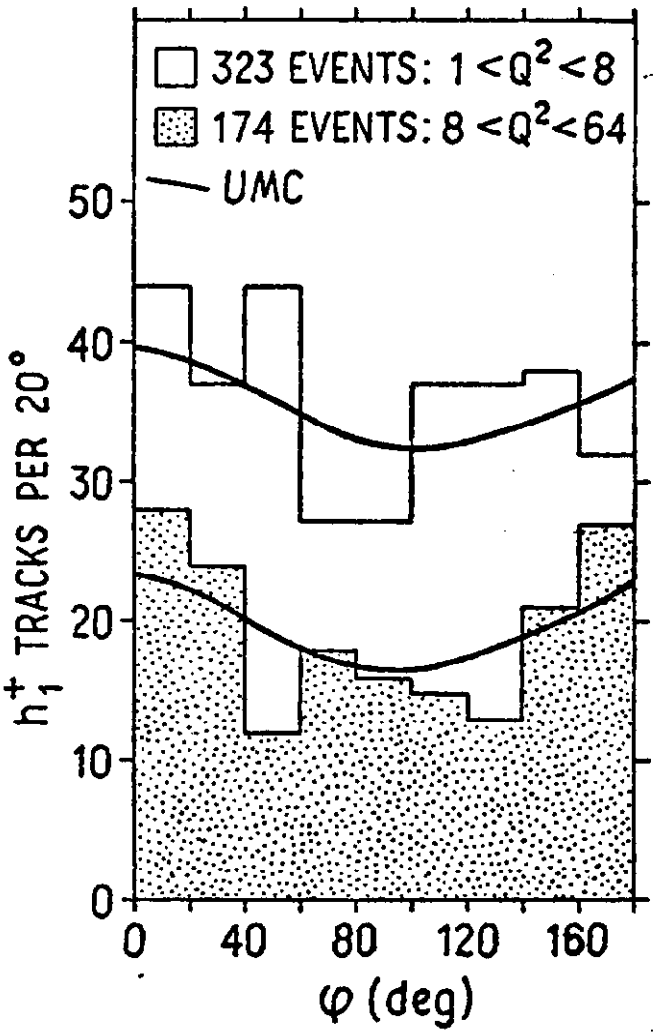
323 EVENTS: 1 < Q² < 8
174 EVENTS: 8 < Q² < 64
UMC
50
40
30
20
10
0
h₁⁺ TRACKS PER 20°
0
40
80
120
160
φ (deg)

Fig. 15

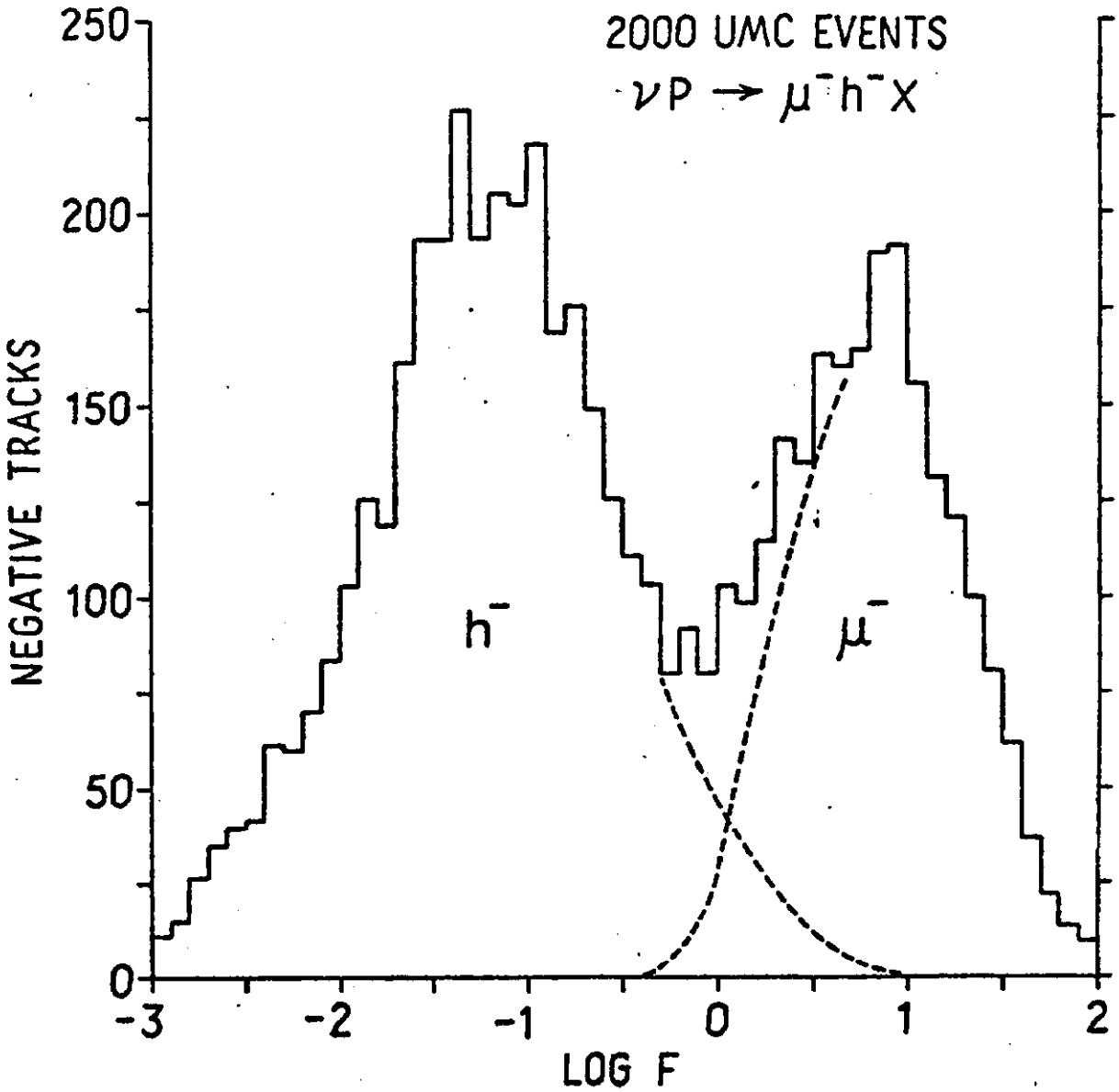
2000 UMC EVENTS
$\nu P \rightarrow \mu^- h^- X$
NEGATIVE TRACKS
250
200
150
100
50
0
h^-
μ^-
-3
-2
-1
0
1
2
LOG F

Fig. A1

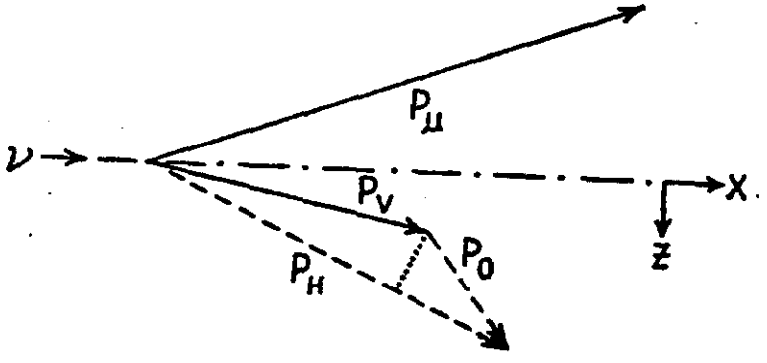

Fig. B1

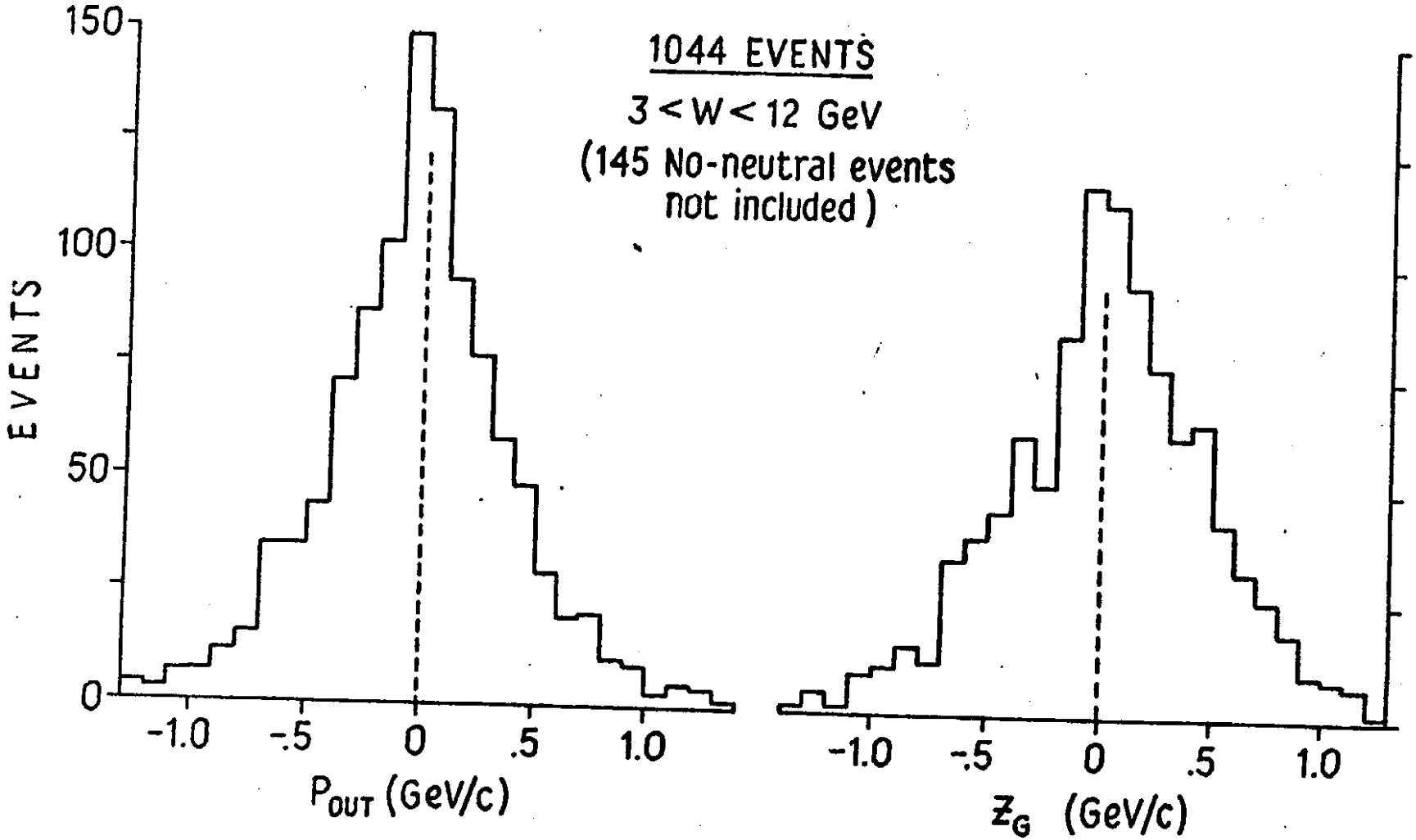
1044 EVENTS
3 < W < 12 GeV
(145 No-neutral events
not included)
EVENTS
150
100
50
0
-1.0
-.5
0
.5
1.0
P_{OUT} (GeV/c)
Z_G (GeV/c)

Fig. B2

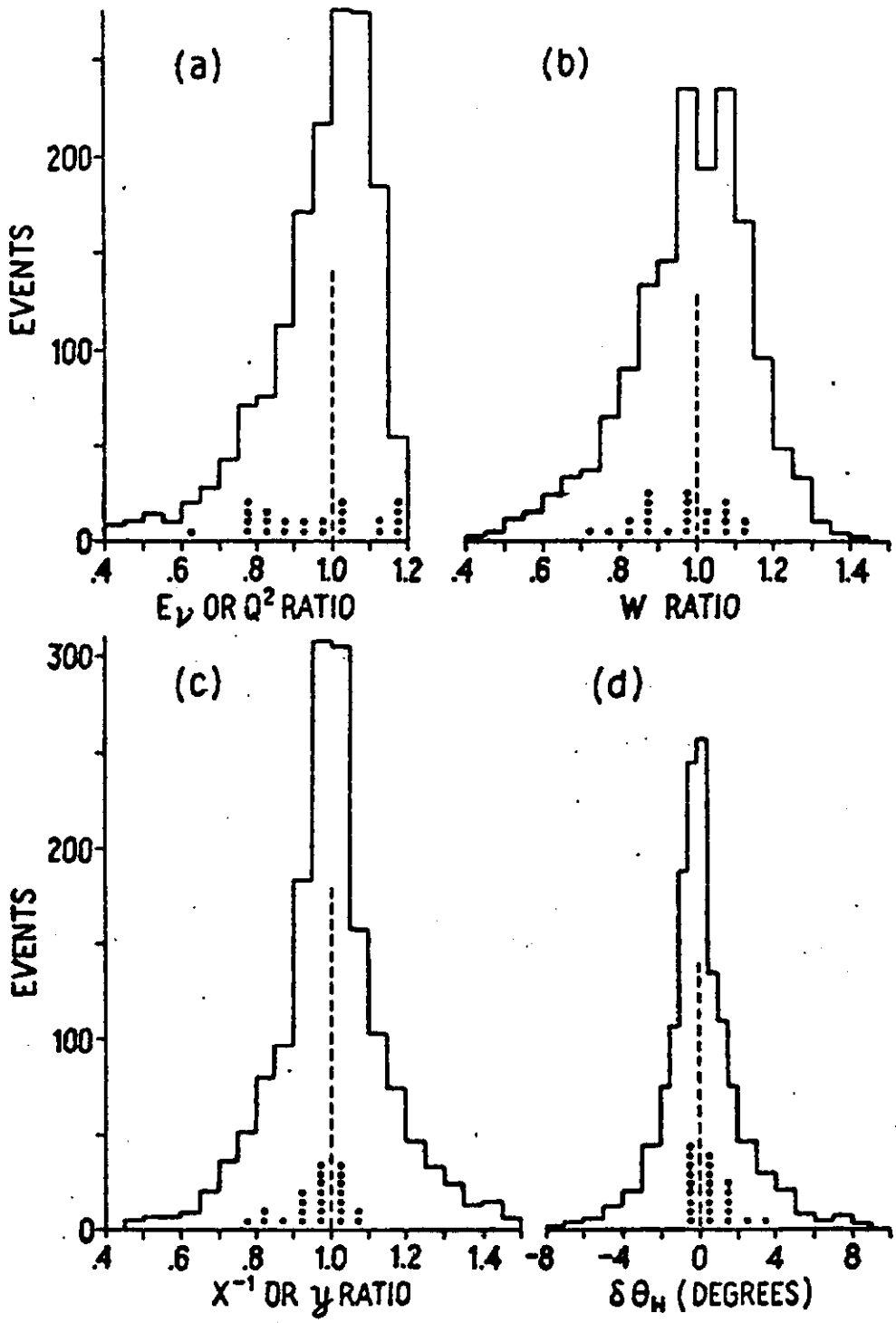
(a)
(b)
(c)
(d)
EVENTS
200
100
0
300
.4
.6
.8
1.0
1.2
1.4
-8
-4
4
8
E_ν OR Q^2 RATIO
W RATIO
X^{-1} OR y RATIO
$\delta\theta_H$ (DEGREES)

Fig. B3